

## Aberystwyth University

### *Fine-Scale Structure in Cometary Dust Tails I:*

Price, Oliver ; Jones, Geraint H.; Morrill, Jeff; Owens, Mathew; Battams, Karl; Morgan, Huw; Druckmüller, Miloslav; Deiries, Sebastian

*Published in:*

Icarus

*DOI:*

[10.1016/j.icarus.2018.09.013](https://doi.org/10.1016/j.icarus.2018.09.013)

*Publication date:*

2019

*Citation for published version (APA):*

Price, O., Jones, G. H., Morrill, J., Owens, M., Battams, K., Morgan, H., Druckmüller, M., & Deiries, S. (2019). Fine-Scale Structure in Cometary Dust Tails I: Analysis of Striae in Comet C/2006 P1 (McNaught) through Temporal Mapping. *Icarus*, 319, 540-557. <https://doi.org/10.1016/j.icarus.2018.09.013>

#### **General rights**

Copyright and moral rights for the publications made accessible in the Aberystwyth Research Portal (the Institutional Repository) are retained by the authors and/or other copyright owners and it is a condition of accessing publications that users recognise and abide by the legal requirements associated with these rights.

- Users may download and print one copy of any publication from the Aberystwyth Research Portal for the purpose of private study or research.
- You may not further distribute the material or use it for any profit-making activity or commercial gain
- You may freely distribute the URL identifying the publication in the Aberystwyth Research Portal

#### **Take down policy**

If you believe that this document breaches copyright please contact us providing details, and we will remove access to the work immediately and investigate your claim.

tel: +44 1970 62 2400  
email: [is@aber.ac.uk](mailto:is@aber.ac.uk)

## Accepted Manuscript

Fine-Scale Structure in Cometary Dust Tails I: Analysis of Striae in Comet C/2006 P1 (McNaught) through Temporal Mapping

Oliver Price, Geraint H. Jones, Jeff Morrill, Mathew Owens, Karl Battams, Huw Morgan, Miloslav Drückmüller, Sebastian Deiries

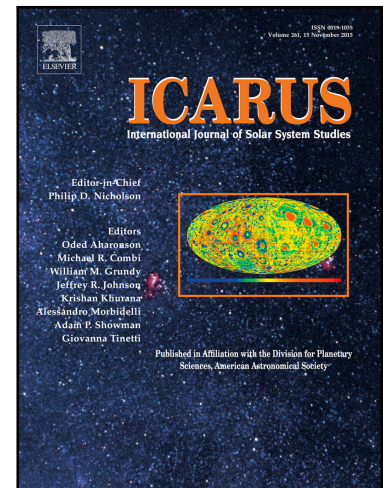
PII: S0019-1035(18)30119-2  
DOI: <https://doi.org/10.1016/j.icarus.2018.09.013>  
Reference: YICAR 13019

To appear in: *Icarus*

Received date: 26 February 2018  
Revised date: 25 July 2018  
Accepted date: 11 September 2018

Please cite this article as: Oliver Price, Geraint H. Jones, Jeff Morrill, Mathew Owens, Karl Battams, Huw Morgan, Miloslav Drückmüller, Sebastian Deiries, Fine-Scale Structure in Cometary Dust Tails I: Analysis of Striae in Comet C/2006 P1 (McNaught) through Temporal Mapping, *Icarus* (2018), doi: <https://doi.org/10.1016/j.icarus.2018.09.013>

This is a PDF file of an unedited manuscript that has been accepted for publication. As a service to our customers we are providing this early version of the manuscript. The manuscript will undergo copyediting, typesetting, and review of the resulting proof before it is published in its final form. Please note that during the production process errors may be discovered which could affect the content, and all legal disclaimers that apply to the journal pertain.



# Fine-Scale Structure in Cometary Dust Tails I: Analysis of Striae in Comet C/2006 P1 (McNaught) through Temporal Mapping

Oliver Price<sup>a,b</sup>, Geraint H. Jones<sup>a,b</sup>, Jeff Morrill<sup>c</sup>, Mathew Owens<sup>d</sup>, Karl Battams<sup>c</sup>, Huw Morgan<sup>e</sup>, Miloslav Drůckmüller<sup>f</sup>, Sebastian Deiries<sup>g</sup>

<sup>a</sup>Mullard Space Science Laboratory, Department of Space & Climate Physics, University College London, Holmbury St. Mary, Dorking, Surrey RH5 6NT, UK

<sup>b</sup>The Centre for Planetary Sciences at UCL/Birkbeck, London, UK

<sup>c</sup>Naval Research Laboratory, Washington, D. C., USA

<sup>d</sup>Space and Atmospheric Electricity Group, Department of Meteorology, University of Reading, UK

<sup>e</sup>Aberystwyth University, Aberystwyth, Wales, UK

<sup>f</sup>Institute of Mathematics, Faculty of Mechanical Engineering, Brno University of Technology, Czech Republic

<sup>g</sup>European Organisation for Astronomical Research in the Southern Hemisphere (Germany)

---

## Abstract

Striated features, or *striae*, form in cometary dust tails due to an as-yet unconstrained process or processes. For the first time we directly display the formation of striae, at C/2006 P1 McNaught, using data from the SOHO LASCO C3 coronagraph. The nature of this formation suggests both fragmentation and shadowing effects are important in the formation process. Using the SOHO data with STEREO-A and B data from the HI-1 and HI-2 instruments, we display the evolution of these striae for two weeks, with a temporal resolution of two hours or better. This includes a period of morphological change on 2007 January 13-14 that we attribute to Lorentz forces caused by the comet's dust tail crossing the heliospheric current sheet. The nature of this interaction also implies a mixing of different sized dust along the striae, implying that fragmentation must be continuous or cascading. To enable this analysis, we have developed a new technique – temporal mapping – that displays cometary dust tails directly in the *radiation beta* (ratio of radiation pressure to gravity) and dust *ejection time* phase space. This allows for the combination of various data sets and the removal of transient motion and scaling effects.

## Highlights

- We directly observe the formation of striated features in a comet's dust tail for the first time at C/2006 P1 McNaught.
- We show how the temporal mapping technique - plotting dust tails in terms of radiation pressure effects against time - aligns features between multiple observations from Earth and spacecraft.
- The striated tail features are shown to remain at the same locations in temporal maps over time, demonstrating the accuracy of the technique.
- The mapping technique highlights a period of morphological change during 2007 January 13-14, which we argue from a comparison with solar wind simulations is from changing Lorentz force effects on dust grains as they cross the heliospheric current sheet.

**Keywords:** Comets, dust, Comets, plasma, Solar wind

---

Email address: oliver.price.15@ucl.ac.uk ()

## 1. Introduction

When active, comets release dust grains of various sizes and morphologies (e.g. Schulz et al. 2015; Hilchenbach et al. 2016). The grains' trajectories are influenced by solar radiation pressure to form dust tails, which lag behind the nucleus's motion about its orbit, e.g. Fulle (2004). Analysis of dust tails' structure can reveal key information on the dust grains' parameters, together with the time of release from the nucleus. These parameters can in turn provide information on the activity of the nucleus.

Features commonly observed in cometary dust (type II) tails include *synchronic bands*, which are large-scale linear features that are coaligned with the position of the comet's nucleus, and, much more rarely, *striae*. The latter are puzzling features that have only been observed in a few, generally very high production rate comets, including C/1957 P1 (Mrkos) (Sekanina, Z, Farrell, 1982), C/1962 C1 (Seki-Lines) (McClure, 1962), C/1975 V1 (West) (Koutchmy and Lamy, 1978; Lamy and Koutchmy, 1979; Nishioka et al., 1992), and C/1996 O1 (Hale-Bopp) (Sekanina and Pittichová, 1997).

Comet C/2006 P1 McNaught – for brevity, from hereon referred to as *McNaught* only – was discovered by Robert McNaught on 2006 August 7 (McNaught, 2006), and reached perihelion on 2007 January 12 at a distance of 0.17 AU from the Sun. This was well inside the perihelion distance of planet Mercury, and therefore a near-Sun comet (Jones et al., 2018). Undoubtedly a modern example of a “Great Comet”, it was easily visible from Earth through much of January 2007, but only from the southern hemisphere when at its most spectacular post-perihelion. The orbit of McNaught suggests it is was a dynamically new comet from the Oort cloud (Marsden, 2007).

Combi et al. (2011) found that the comet's water production rate could be approximated by  $5.4 \times 10^{29} r^{2.4} \text{ s}^{-1}$ , where  $r$  is the heliocentric distance, and that it reached a peak of  $5.48 \times 10^{31} \text{ molec s}^{-1}$  on 2007 January 13. Despite the comet's spectacular appearance around perihelion, relatively few works have been published on it based on visible wavelength observations, largely due to the difficulty in observing the object with ground-based facilities, though ground-based observations of sodium emission from the comet were possible with a solar telescope (Leblanc et al., 2008). The comet had an extensive, highly structured dust tail, displaying many striae. Observations of the comet at infrared wavelengths reveal that it had larger and more compact porous grains than many other objects (Kelley et al., 2010; Wooden et al., 2014).

Here we report on the analysis of the striae observed in McNaught, which arguably possessed the most spectacular dust tail of recent times, and certainly the one for which is available the most comprehensive collection of observations to date. We apply a new reprojection technique, which we refer to as *temporal mapping*, to images of McNaught's dust tail acquired from several sources, allowing us to track the behaviour of striae in the comet's tail throughout the comet's perihelion passage.

We present a sequence of images captured by the *Large Angle and Spectrometric Coronagraph (LASCO)* on the ESA/NASA *Solar and Heliospheric Observatory (SOHO)* spacecraft, that appears to record clearly for the first time the formation of several striae. Together with data from the the *Heliospheric Imagers (HI)* that form part of the wider *Sun-Earth Connection Coronal and Heliospheric Investigation (SECCHI)* remote sensing package on the twin NASA *STEREO-A* and *B* spacecraft, we track the formation and evolving appearance of numerous striae. We propose that the progressive realignment of many of these striae is due to interactions between electrically charged dust grains and the heliospheric magnetic field.

### 1.1. Striae Formation Theories

Most striae models describe formation through the fragmentation of larger dust particles. In addition to gravity, cometary dust grains are certainly strongly influenced by radiation pressure. As these two primary forces act in opposition to each other, the effective force acting on them is equivalent to *reduced gravity*. This is parametrised by the dimensionless constant  $\beta_r$ , given as:

$$\beta_r = \frac{\text{Radiation Force}}{\text{Gravitation Force}} \quad (1)$$

The fragmentation of grains leads to the spreading of dust grains over time due to a difference in the  $\beta_r$  parameter between individual particles.

Sekanina and Farrell (1980) proposed that stria formation is a two-step process. They posited that the striae's parent dust grains are released from the nucleus all with similar values. After a delay, these grains break up within a short period of time. Their fragments have a range of  $\beta_r$  values, and radiation pressure separates the grains according

to  $\beta_r$ , forming near-linear structures. Under this scenario, along a single stria, there is expected to be a monotonic increase in  $\beta_r$  with increasing heliocentric distance.

This model has been found to agree well with observations of striae (e.g. Pittichová et al. 1997). However, there is a serious issue with the Sekanina and Farrell two-step fragmentation scenario, in that it is difficult to explain why parent grains would all fragment after approximately the same time delay. They suggested rotational bursting generally due to uneven radiation pressure over grains' surfaces, but this has not been widely accepted. Hill and Mendis (1980) suggested that the fragmentation of grains could occur due to electrostatic charging, with the few keV and more electrons required for this process originating in the closed current system of the induced cometary magnetotail.

Nishioka and Watanabe (1990) and Nishioka (1998) proposed a different scenario for the formation of striae. Rather than a two-step process, an almost continuous cascade of fragmentation was proposed. This cascade continues beyond where grains become too small to observe. This process would result in fragments of all values co-existing along the length of each stria. Sekanina and Pittichová (1997) pointed out that a relaxed fragmentation time should lead to wedge shaped striae, which are not observed.

Other models have also been proposed. These include those of Froehlich and Notni (1988) and Notni and Thoenert (1988), who suggested stabilising effects due to optical thickness of dust clouds. Steckloff and Jacobson (2016) considered that each stria is the result of the destruction of macroscopic sized (10 - 100m) boulders by rotational stresses from sublimation pressures.

## 2. Data

Around perihelion, McNaught's proximity to the Sun in the sky made ground-based observations particularly challenging. However, instruments aboard the SOHO, STEREO-A, and STEREO-B spacecraft provided excellent imaging data, allowing the comet's coma and tail structures to be monitored through the perihelion passage. The activation of the *SECCHI* heliospheric imagers aboard the then-recently launched twin *STEREO* spacecraft came just in time to capture the dust tail as the comet reached perihelion, and this event was also captured by the *SOHO LASCO C3* coronagraph.

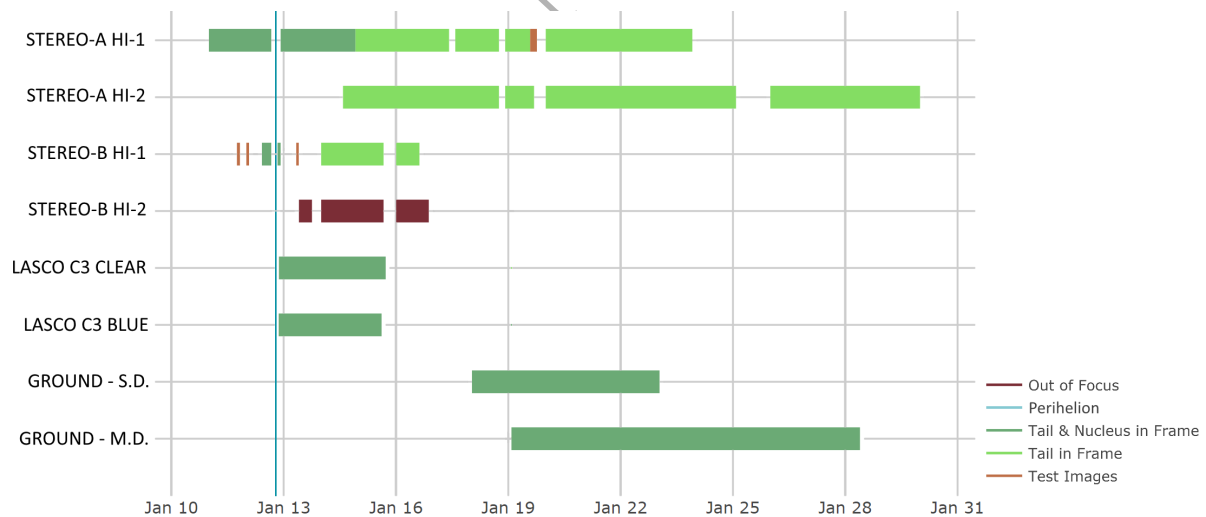


Figure 1: Gantt chart summarising observations from all sources, including the different instruments aboard the STEREO-A, STEREO-B and SOHO spacecraft, and ground based images from authors S.D. and M.D.

The comet was well observed from Earth from the southern hemisphere post-perihelion, with some of the older dust features also seen in the northern hemisphere during the same period, despite the nucleus being below the horizon from those locations. We note that this is similar to the circumstances of Comet de Chéseaux (C/1743 X1) with its extensive, structured dust tail (Kronk, 1999). For this project we use the *SECCHI HI-1* and *HI-2* datasets from both

78 *STEREO* spacecraft, as well as *LASCO C3* Clear and Blue filter data and various ground-based images. Figure 1  
 79 summarizes the images obtained from all sources. Further details of each data source are provided below.

### 80 2.1. Stereo A SECCHI HI

81 The twin NASA *STEREO* spacecraft follow separate orbits around the Sun, moving progressively ahead of and  
 82 behind the position of the Earth (Howard et al., 2008). Each spacecraft has two Heliospheric Imagers, *HI-1* and  
 83 *HI-2*. These consist of CCD cameras pointed off axis from the sun. *HI-1* points closest to the sun with a field of  
 84 view of  $20^\circ$  and solar offset of  $14^\circ$  (Eyles et al., 2009). The effective primary bandpass of the instrument is  $\sim 630$ –  
 85  $730$  nm, with additional, weaker coverage of the wavelengths  $\sim 300$ – $450$  and  $\sim 900$ – $1000$  nm (Bewsher et al., 2010).  
 86 Images are obtained onboard measuring 2048 pixel square, but were downsampled to 1024 pixel square images for  
 87 transmission during the period of interest. The pixel scale of transmitted images is  $70''$  pixel $^{-1}$ . This corresponded  
 88 to a physical resolution of 43 000 km at McNaught's head at perihelion. As the dust tail extended from the nucleus  
 89 towards *STEREO-A*, the physical resolution for the tail was higher, reaching  $\sim 33$  000 km pixel $^{-1}$ .

90 At the time of the McNaught observations, both *HI-1* instruments were being commissioned, and McNaught was  
 91 serendipitously in the field of view as their observations on both spacecraft began. A few 2048 pixel-wide images  
 92 were downlinked during commissioning, but given the large scale of the striae, these do not prove particularly useful  
 93 for this purpose compared to the 1024 pixel-wide images. The data from this instrument were inferred to imply the  
 94 presence of a neutral iron tail at McNaught (Fulle et al., 2007).

95 Figure 2 shows an example image of McNaught from *STEREO-A HI-1*. The fine structure of the dust tail is clear,  
 96 but several artefacts also appear. The *HI* imagers are primarily designed to image sunlight Thomson scattered by  
 97 tenuous solar wind and transient structures within it, such as coronal mass ejections. The instrument is not designed  
 98 to deal during standard operations with objects that are as bright as McNaught, hence much of the region around the  
 99 coma is overexposed. The particularly bright coma of McNaught caused significant CCD bleeding. Furthermore,  
 100 as the *HI* cameras do not have shutters (Eyles et al., 2009), as the pixel values are read off the detector, the camera  
 101 continues to collect light, causing the bright background in parts of the image adjacent to the brightest tail regions.

102 The sequence of raw data from *HI-1* can be viewed here:

103 Uploaded Media: [hi-1.gif](#)

104 With the Multiscale Gaussian Normalisation enhanced version (see section 2.4.1 for details) viewable here:

105 Uploaded Media: [hi-1-mgn.gif](#)

106 The second of the two heliospheric imagers, *HI-2*, points further off axis with a field of view of  $70^\circ$  and solar offset  
 107 of  $53.7^\circ$ , with the instrument designed to image CMEs all the way to the Earth (Eyles et al., 2009). The bandpass of  
 108 *HI-2* is centered on  $\sim 640$  nm, with a FWHM of  $\sim 450$  nm (Tappin et al., 2015). The pixel scale of transmitted *HI-2*  
 109 images is  $4'$  pixel $^{-1}$ , which corresponds to a physical scale at McNaught varying between 90 000 and 200 000 km,  
 110 depending on the position in the dust tail.

111 Although the nucleus of the comet did not pass into the *HI-2* field of view, the extensive tail was present in the  
 112 instrument data for approximately two weeks. Figure 3 shows an example view of McNaught from *STEREO-A HI-2*.  
 113 Here the fine structure of the tail is much dimmer than in *HI-1* images. Complicating the interpretation of some of the  
 114 images is the presence of zodiacal dust, whose surface brightness is comparable to that of the striae.

115 The sequence from *HI-2* (difference image enhanced as per 2.4.2) can be viewed here:

116 Uploaded Media: [hi-2-diff.gif](#)

### 117 2.2. STEREO B SECCHI HI

118 The *HI* instrument aboard *STEREO-A* has the same properties as its sister spacecraft, and both spacecraft were  
 119 still very close to the Earth-Moon system at the time. The instrument door on *STEREO-B* opened for the first time on  
 120 January 11, so the instrument was in a much earlier stage in its commissioning than its counterpart on *STEREO-A*.  
 121 Many of its images contain artefacts, and there are fewer images taken at regular intervals. The default FITS headers  
 122 for providing the celestial coordinates provided inconsistent results compared to the background starfields, so the

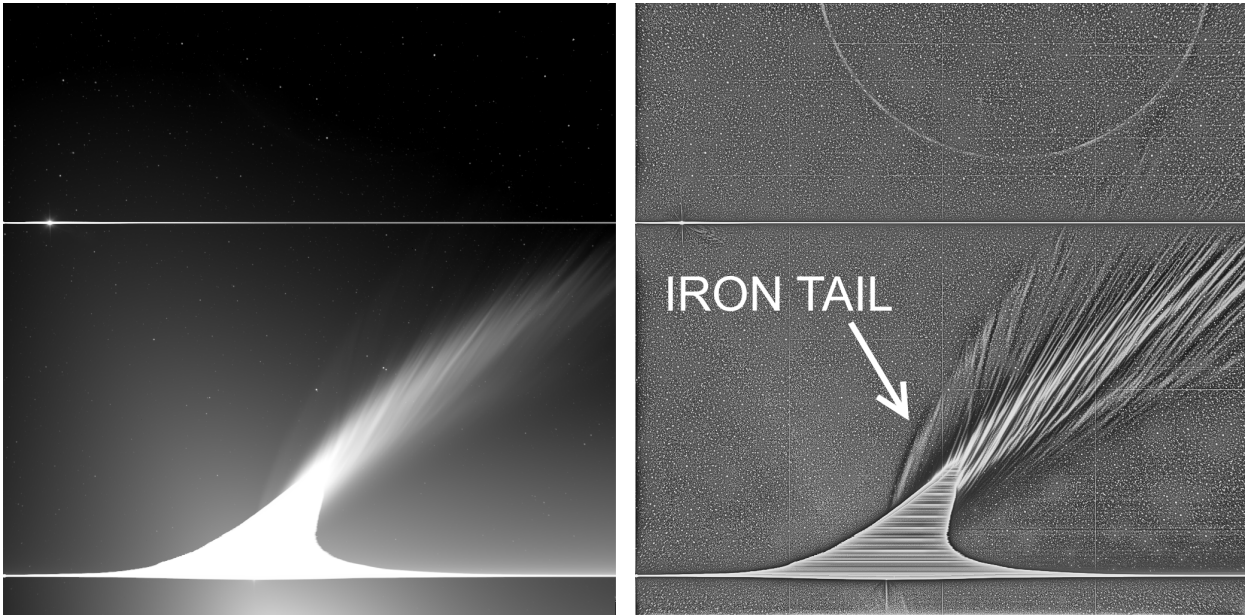


Figure 2: (Left) The view of C/2006 P1 McNaught from STEREO-A HI-1 on 2007 January 14 at 00:01. The sun is centre below relative to both images (rotated 90° clockwise from nominal orientation). Apparent are several issues for the purpose of studying this comet, including the background intensity of the zodiacal dust at the bottom of the image, as well as overexposure and CCD bleeding around the nucleus and bright apparition of Venus (bright feature at upper left). (Right) The same image, enhanced with Multiscale Gaussian Normalisation. The process enhances fine-scale structure in the tail and the faint iron tail, as well as some artifacts, such as the semicircular feature at top, caused by an internal reflection in the instrument.

123 astrometry for the files was recalculated independently using the automated service at *astrometry.net* (Lang et al.,  
124 2010).

125 We note in passing that true stereo images of Comet McNaught were taken by SECCHI HI-1A and HI-1B nineteen  
126 times between January 12 and 15. An example pair, from 00:01 on January 14, can be seen in Figure 4. The parallax  
127 effect is clear in the two images, with a  $\sim 0.3^\circ$  shift in background star positions. The separation of the two spacecraft  
128 was however too small to provide useful information on the three-dimensional distribution of the cometary dust to be  
129 extracted, e.g. to confirm that the dust lay exclusively in the comet's orbital plane.

130 The HI-2 instrument aboard STEREO-B also captured the edge of the extended tail of McNaught. However, the  
131 instrument was unfortunately not in focus at this time and so this dataset was disregarded.

### 132 2.3. SOHO LASCO C3

133 The SOHO spacecraft resides  $\sim 1$  million km sunward of Earth at Sun-Earth Lagrange Point L1. Its LASCO  
134 coronagraph images a  $15^\circ$  wide circle surrounding the Sun (Brueckner et al., 1995), and is responsible for the greatest  
135 number of comet discoveries (Battams and Knight, 2017). LASCO comprises three instruments; all the McNaught  
136 data were gathered using coronagraph C3, which covers 3.7 to 30 solar radii from the Sun's centre, recorded on  
137 1024 by 1024 pixel images at a spatial resolution of  $56 \text{ arcsec pix}^{-1}$ . Further technical information on the LASCO  
138 instrument and its calibration is covered by Morrill et al. (2006).

139 Most McNaught images were gathered using a broadband “clear” filter covering wavelengths of 400 to 850 nm.  
140 These images, whilst capturing a great degree of detail in the dust tail, were overexposed in the comet's near-nucleus  
141 and coma regions. They suffer issues with overexposure of McNaught's bright nucleus, although the effect is less  
142 severe than with the STEREO heliospheric imagers. The instrument also includes 5 other narrower wavelength range  
143 filters (Morrill et al., 2006). As has also occurred with other anticipated bright comets, LASCO was commanded to  
144 obtain numerous images using the color filters when McNaught was within the C3 field of view. In order to maximize  
145 data return, these images only included subframes of the entire C3 field of view, and were compressed onboard using  
146 a lossy algorithm prior to transmission to Earth. Despite the lower quality of these images compared to the clear

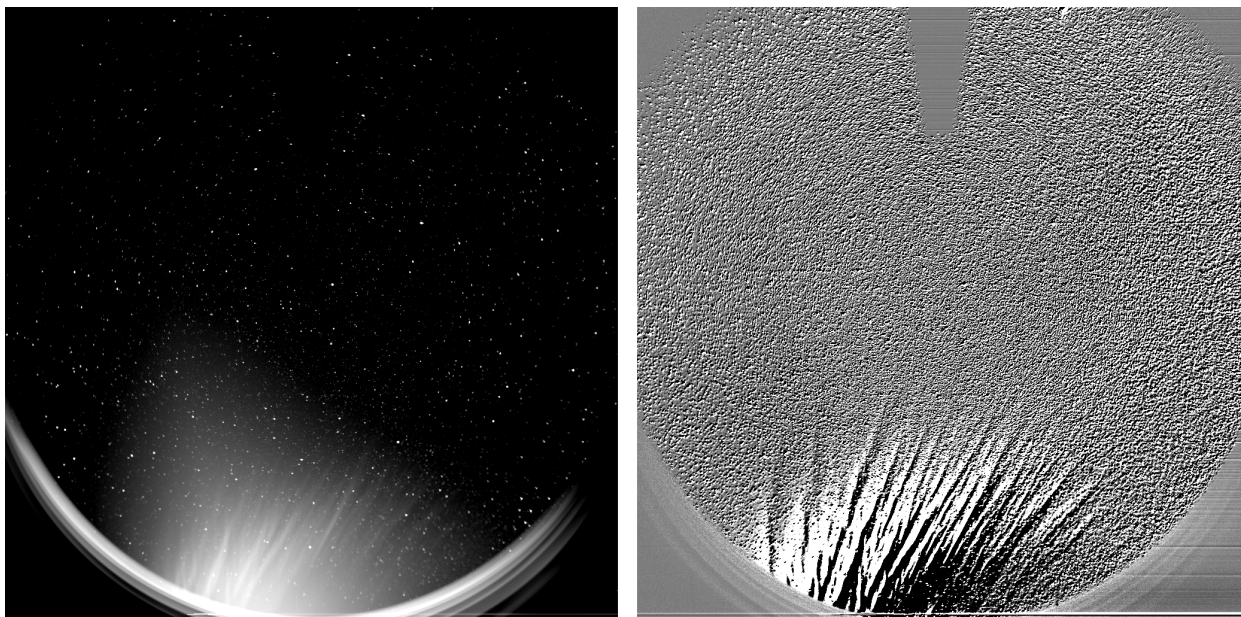


Figure 3: (Left) The view of McNaught's dust tail from STEREO-A HI-2 on the 2007 January 19 at 00:01. The HI-1 frame and sun are below the image (rotated 90° clockwise from nominal orientation). The zodiacal dust is of comparable brightness to striae. (Right) A difference image of same frame. This image has been made by subtracting the preceding frame obtained 2 hours earlier.

147 images, they are very valuable for the study of the striae, as they record structures much closer to the comet's nucleus  
 148 than in images obtained using the clear filter, which were generally overexposed around the comet's head. Although  
 149 the clear filter images were least affected by data compression artifacts, much of the analysis of LASCO data here  
 150 concentrates on images obtained using the instrument's blue filter.

151 The LASCO C3 Clear data was used with several calibration algorithms already applied, referred to as Level 1  
 152 calibration. These calibration steps include corrections for the flat field response of the detector, radiometric sensi-  
 153 tivity, stray light, geometric distortion, and vignetting (Morrill et al., 2006). Unfortunately for the Blue filter dataset,  
 154 Level 1 calibration is not available, and the raw level 0 data had to be used instead. In this analysis, as we concentrate  
 155 on the morphology and dynamics of tail features and do not rely on any absolute calibration of the images, we deemed  
 156 the unprocessed Level 0 images to be of sufficient quality for this study. This does however mean that the Sun's dust  
 157 (F) corona and stray light are present in these images, but these largely structureless background features were largely  
 158 removed by the enhancement techniques described below

159 Figure 5 shows a LASCO clear filter image of the comet, enhanced with multiscale gaussian normalisation (Sec-  
 160 tion 2.4.1). McNaught's nucleus was within the LASCO C3 field of view from 2007 January 12 01:42 UT to January  
 161 15 21:54 UT. The sunward edge of the dust tail remained in the field of view for several hours after the nucleus left,  
 162 but with no clearly discernible structures visible within it.

163 The LASCO clear filter sequence (MGN enhanced as per 2.4.1) can be viewed here:

164 `Uploaded Media:soho_mgn_gif.gif`

165 Figure 6 shows a combination of imaging data from SOHO LASCO and STEREO SECCHI HI-1 and HI-2,  
 166 demonstrating the relative scales of the images returned by the different instruments.

#### 167 2.4. Enhancement techniques

168 The dust tail striae are features present over a wide dynamic range in the images. Enhancement techniques were  
 169 found to be required to trace the positions of the striae, and to also address the presence of zodiacal light in the images,  
 170 i.e. the extension of the F corona. Two complementary enhancement techniques were employed. In presenting the  
 171 enhanced images in this paper, as the brightness scale is largely arbitrary, we do not provide quantitative brightness  
 172 values.



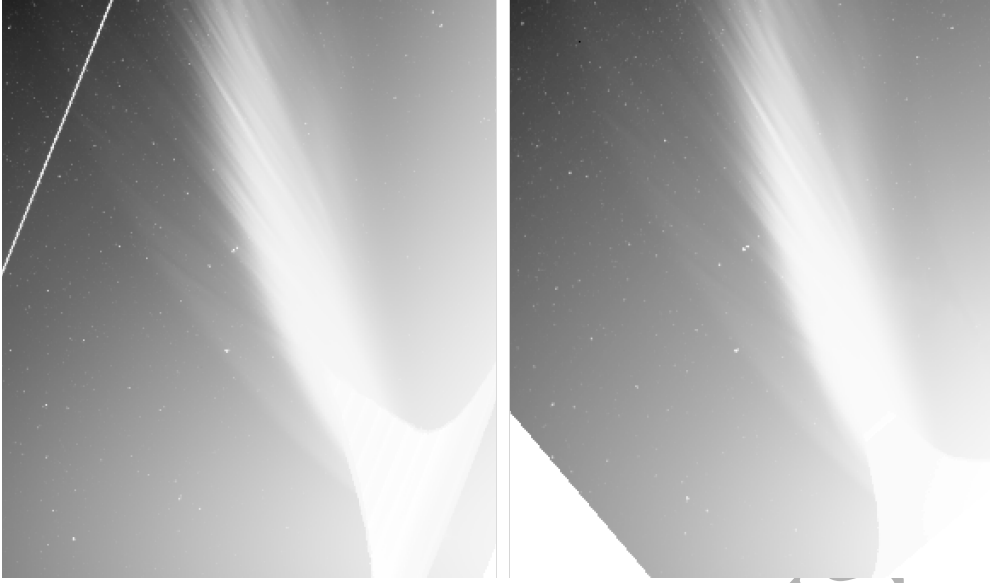


Figure 4: A true stereo image pair of McNaught from STEREO-A (left) and STEREO-B (right) on 2007 January 14 at 00:01. The images have been rotated such that ecliptic north is upwards in both, and displayed with a histogram equalization-based brightness scaling.

#### 173 2.4.1. Multiscale Gaussian Normalisation

174 The large range in brightness over the tail region makes it difficult to extract fine structure information over  
 175 the whole range of intensities and physical scales, even with the use of logarithmic brightness scaling. Morgan  
 176 and Druckmüller (2014) developed the Multiscale Gaussian Normalisation technique, MGN, for application to such  
 177 situations. At several length scales, convolution of the image with Gaussian kernels enables the calculation of local  
 178 means and variance. These are used to offset and normalise pixel values locally to a mean of zero and unity standard  
 179 deviation. The set of normalised images are then recombined into a global image, where fine structure across all parts  
 180 of the image are visible. Figure 2 shows the success of this method for revealing fine structure in cometary dust tails.  
 181 The process is very efficient, working in a matter of seconds. We use this technique here for all three datasets.

#### 182 2.4.2. Difference images

183 In certain cases MGN enhancement fails to enhance fine detail, probably due to noise. After the comet left the  
 184 field of view of the *SECCHI* Heliospheric imagers, striae persisted in the tail and gradually faded from view. The  
 185 features could eventually no longer be resolved by eye, even with MGN enhancement. However, difference images  
 186 created by subtracting the previous image frame from each image reveal faint fine structure. This allows us to extend  
 187 the useful range of data by several days.

#### 188 2.5. Ground Based Data

189 The comet reached a peak magnitude of  $-5.5$  (Marsden, 2007), when it was visible in the daylight sky near the Sun.  
 190 Post-perihelion, it was easily visible to the naked eye in the southern hemisphere, when the nucleus was not observable  
 191 from north of the equator. Some older striae were however visible from the northern hemisphere during that period.  
 192 Many professional and amateur astronomers photographed the object. Here we have used wide angle photographs  
 193 taken by author Sebastian Deiries at the European Southern Observatory in Chile, and wide angle photographs and  
 194 composites taken by author Miroslav Drückmüller in Chile and Argentina.

### 195 3. Methodology

#### 196 3.1. Motivation

197 Dust tail structures have traditionally been investigated using Monte-Carlo models of dust populations, and com-  
 198 paring the results directly to images of comets. Many such studies have been successful, but these approaches do

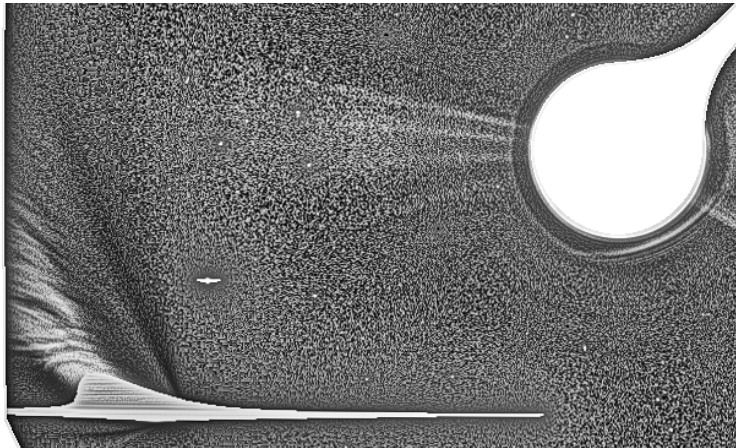


Figure 5: The view of McNaught from the SOHO LASCO C3 coronagraph, using the clear filter, on January 15 at 00:53 UT. The image has been enhanced using the MGN technique (Section 2.4.1). The bright object near the comet is Mercury. Celestial north is up.

199 have limitations. Kharchuk and Korsun (2010) reported on their efforts to model the striae visible in McNaught's tail.  
 200 The results were somewhat satisfactory, but failed to reproduce the correct orientation of the striae, which in their  
 201 simulations were aligned with the position of the comet's nucleus, and were therefore synchronic bands caused by  
 202 variations in dust release rates at the nucleus.

203 Traditionally synchronic and syndyne lines are plotted alongside on overlaid onto images, which does allow for the  
 204 model to be intuitively matched to the tail by eye. However, this method suffers due to the compression of lines near  
 205 the nucleus, and rarefaction in the furthest and oldest regions of the tail. It is therefore difficult to relate dust features  
 206 in these regions to one another, particularly across long time sequences where near nucleus features may have traveled  
 207 out and reached the far tail, and especially when the viewing geometry or instrument has changed.

208 We introduce here a new dust tail analysis technique which presents dust features in a consistent way, by morphing  
 209 images of comets onto a matrix of assumed dust age and sensitivity to solar radiation pressure. This temporal mapping  
 210 technique has several advantages:

- 211 1. A single dust tail feature can be analyzed over an extended period of time, despite changes in its physical scale,  
 212 transient motion and viewing orientation
- 213 2. Changes in the dust tail during periods when the appearance of a tail changes rapidly can be easily resolved
- 214 3. Issues concerning observing geometry are removed, e.g. when the observer is close to the orbital plane of the  
 215 comet and dust tail features are foreshortened
- 216 4. Images of an individual comet tail obtained by different observers can be easily compared
- 217 5. Important additional parameters, such as heliocentric distance, orbital plane coordinates and dust phase angle  
 218 can be considered and evaluated for the observations

219 We have implemented the temporal mapping technique in Python, as detailed below. As McNaught was a very bright,  
 220 high activity comet for which we have high quality dust tail imaging data, it is a perfect subject for the application of  
 221 the technique.

### 222 3.2. The Finson Probstein model

223 The Finson-Probstein model provides a good basis for cometary dust tail modelling (Finson and Probstein, 1968).  
 224 This assumes that only gravity and radiation pressure act on the dust grains after their release from the nucleus. Using  
 225 the parameter  $\beta_r$  introduced in Section 1.1, an equation of motion for a dust particle can be based on the acceleration  
 226  $a$ , defined by:

$$a = \frac{-GM_s(1 - \beta_r)}{r^2} \quad (2)$$

Where  $r$  is the heliocentric distance,  $a$  the acceleration of the dust outwards in the heliocentric radial direction,  $G$  the gravitational constant and  $M_s$  the solar mass. We make several assumptions in our use of the model:

1. The dust is ejected with zero velocity relative to the comet and hence the physics only evolves in two dimensions; the dust tail structure remains entirely in the orbital plane of the comet. Whilst the sublimating gas in reality imparts a velocity to the dust grains, the initial motion is smaller than the velocity imparted by radiation pressure and gravity. Studies of comets at orbital plane crossings show that the bulk of the dust tail remains close to the orbital plane to a reasonable approximation. However, there is some initial sorting of grain size due to smaller particles being accelerated to higher speeds before decoupling from the outflowing gas. As we assume the dust is sorted by the time it reaches the far tail, this is not significant.
2. The value of  $\beta_r$  is constant for a particular dust particle. As dust fragments or sublimates, the value of  $\beta_r$  will be affected. Striae models that include fragmentation and its effects are discussed in section 1.1.
3. The optical thickness of the dust cloud does not affect the  $\beta_r$  value over time.

Note that our technique makes no assumptions about the mass or the physical cross-section of the individual dust grains. We only define a  $\beta_r$  value for each grain.

These assumptions reduce the problem to two parameters:  $\beta_r$ , and the time of dust particle emission, denoted by  $t_e$ . Each image is therefore deterministic, where every combination of  $\beta_r$  and  $t_e$  values maps to a unique position in the tail.

### 3.3. Creating a temporal map

Creating a temporal map requires the following:

1. Astrometry for the image; effectively right ascension,  $RA$ , and declination,  $dec$ , for every pixel. For spacecraft data in FITS format this is often accessible in the FITS metadata. For ground based images it can usually be determined using the *astrometry.net* website (Lang et al., 2010).
2. Orbital ephemerides for the comet and its observer location relative to the sun. We use ephemerides from NASA's JPL Horizons system (Giorgini et al., 1997). A one minute temporal resolution is used to guarantee positional accuracy.
3. The time of the image. For spacecraft data this is known, and many ground based observers provide this with their images. Otherwise it is necessary to manually calculate this by using the celestial coordinates of the comet. If the astrometry for the background image is correct, then the exact position of the comet in the image and thus its location along its orbit can be used together with the orbit ephemeris to calculate the time at which an image was taken.

For a desired mapping with a known range of  $\beta_r$  and  $t_e$ , a temporal map is produced as follows:

1. Perform a trajectory simulation for each required  $\beta_r$  and  $t_e$  value. Using the  $t_e$  value, the corresponding initial condition of the comet is found. The dust is then numerically modelled using the following differential equations, which are adapted from equation 2:

$$\frac{d}{dt} \begin{pmatrix} \vec{r} \\ \vec{v} \end{pmatrix} = \begin{pmatrix} 0 & 1 \\ -\frac{GM_s(1-\beta_r)}{|\vec{r}|^3} & 0 \end{pmatrix} \begin{pmatrix} \vec{r} \\ \vec{v} \end{pmatrix} \quad (3)$$

To solve the numerical equation, we use the 4<sup>th</sup> order Runge Kutta method (Karim, 1966). The dust motion is calculated up until the light travel corrected time of the dust is exactly that at which the image was taken.

2. Once all the values are calculated and converted to  $RA$  and  $dec$ , the Finson-Probstein grid can be plotted over the image to give a visual check that the correct parameters have been used.
3. For each unique position in the image corresponding to particular values of  $\beta_r$  and  $t_e$ , a pixel value is extracted from the image. We convert the  $RA$  and  $dec$  coordinates of each modelled dust grain back into image coordinates using the FITS metadata, and linearly interpolate the four pixel values (from the four pixel centres that form the box containing the converted image coordinates) to get a pixel value for each  $\beta_r$  and  $t_e$ . We plot these pixel values with  $\beta_r$  on the new Y axis. The date and time of each  $t_e$  value is plotted on the X axis, for a selected range of dates.

271 For observations over several days, dust tail features can be held static in the temporal map, showing the evolution  
 272 over time without relative motion effects from observer or comet. Furthermore, with multiple datasets, these maps  
 273 can be mosaicked together. This allows not only for a comparative study of the same features observed with different  
 274 instruments, but also for the dynamic range of the temporal map to be extended beyond the scope of single instruments.

### 275 3.4. Limitations

276 It is important to note that in producing the the temporal maps, whilst the method does preserve the relative  
 277 brightnesses of various parts of the tail, it does distort the relative apparent proportions of pixels with particular  
 278 brightnesses. It is not therefore a tool for accurate photometric analysis, nor was it meant to be one.

279 In addition, we do not account for the strong phase angle dependencies encountered when observing forward  
 280 scattered light, which contributes to the relative brightness gradient across the dust tail. Our method is not suitable for  
 281 extracting dust size distributions, as we do not preserve the photometry nor consider the third dimensional aspect of  
 282 the tail, e.g. Fulle (2004).

## 283 4. Results

### 284 4.1. Overview of McNaught Tail Features

285 From Earth and the cluster of spacecraft surrounding it, the orbit plane angle was  $\sim 25^\circ$  at the start of observations  
 286 on 2007 January 11, rising to a maximum of  $\sim 35^\circ$  on January 16. This good viewing geometry, well outside the  
 287 comet's orbital plane, allowed for the distinctive fan shape of the dust tail to be observed from Earth. At its most  
 288 extensive, McNaught's tail reached visible lengths of just under 1 AU; on January 25, 15 day old dust of  $\beta_r \sim 2$   
 289 extended to 0.975 AU from the nucleus.

290 The tail displayed a bimodal size distribution. Studying the dust maps with unprocessed data, the two peaks of  
 291 this distribution appear centered on  $\beta_r \sim 0.7$  and  $\sim 1.3$ .

292 The dust structures in the bimodal striated tail were generally visible for 12-16 days, although dust at lower  $\beta_r$ , that  
 293 was 24 days old could be discerned in difference images from STEREO-A HI-1. Using a combination of STEREO  
 294 and ground based data (Figure 7), a temporal map (Figure 8) was produced showing three weeks' worth of dust being  
 295 visible on 2007 January 21.

### 296 4.2. Striae Morphology

297 Using the STEREO-A HI-1, HI-2 and the SOHO LASCO C3 Clear filter datasets, a sequence of 339 temporal  
 298 maps was created, showing the main dust tail; i.e.  $0.2 \leq \beta_r \leq 3$ , from 2007 January 11 00:00 UT until January 25  
 299 02:00 UT. This sequence is available as an animation at the following link:

300 Uploaded Media: `main_striae_evolution_sequence.gif`

301 Some selected frames from this sequence are shown in Figure 9.

302 First, we note that all dust tail structures appear clearly and remain stationary with respect to both apparent nucleus  
 303 release time and  $\beta_r$  in the temporal maps, which indicates the success of the method. Although striae generally  
 304 appear linear in the original images, their profiles are curved in the projections presented here. The logarithmic  $\beta_r$   
 305 scale removes some of the curvature, allowing easier analysis of the features. If the striae had originated as nuclear  
 306 outbursts, then they would appear as vertical features in the temporal maps, i.e. dust in each stria being of all the same  
 307 apparent age. As expected based on earlier studies, striae instead appear inclined in these projections, implying that  
 308 they do not form as near-instantaneous outbursts of dust of varying  $\beta_r$  at the nucleus. The slope of the features implies  
 309 that the highest  $\beta_r$  dust in each stria is youngest, and the lowest  $\beta_r$  particles the oldest. This interpretation is however  
 310 dependent on a nucleus source.

311 The lowest  $\beta_r$  particles being the oldest sections of each stria is consistent with fragmentation of larger (generally  
 312 lower  $\beta_r$ ) grains leading to the release of lower mass (generally higher  $\beta_r$ ) particles.

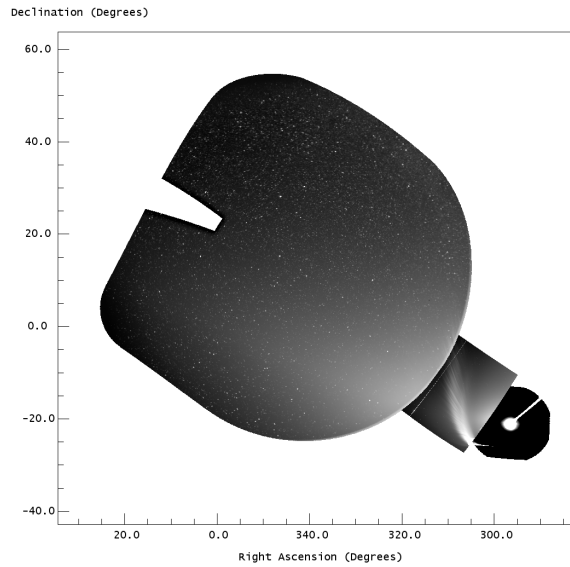


Figure 6: The view of the comet as seen from STEREO and SOHO on 2007 January 15 at 12:00 UT. The SOHO LASCO C3 field of view is the region at lower right centered on the Sun. STEREO SECCHI HI1-A is the tilted square image containing the bulk of the comet's dust tail. The STEREO SECCHI HI2-A image is the leftmost panel, containing the outermost fringes of the dust tail, with the zodiacal light also apparent.

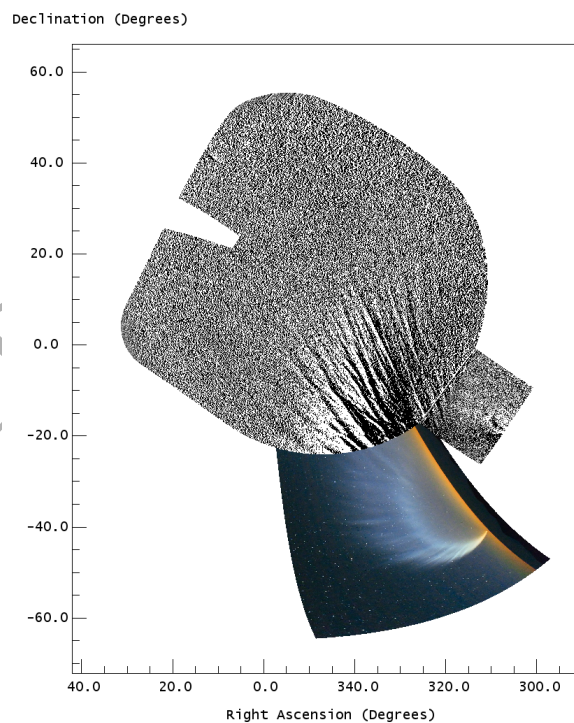


Figure 7: The view of the comet as seen from STEREO and Earth on 2007 January 21 at 01:00 UT, in STEREO SECCHI HI1-A and HI2-A (both frames enhanced by subtraction of the preceding images to enhance differences), and a colour image taken from the European Southern Observatory, Chile by author SD.

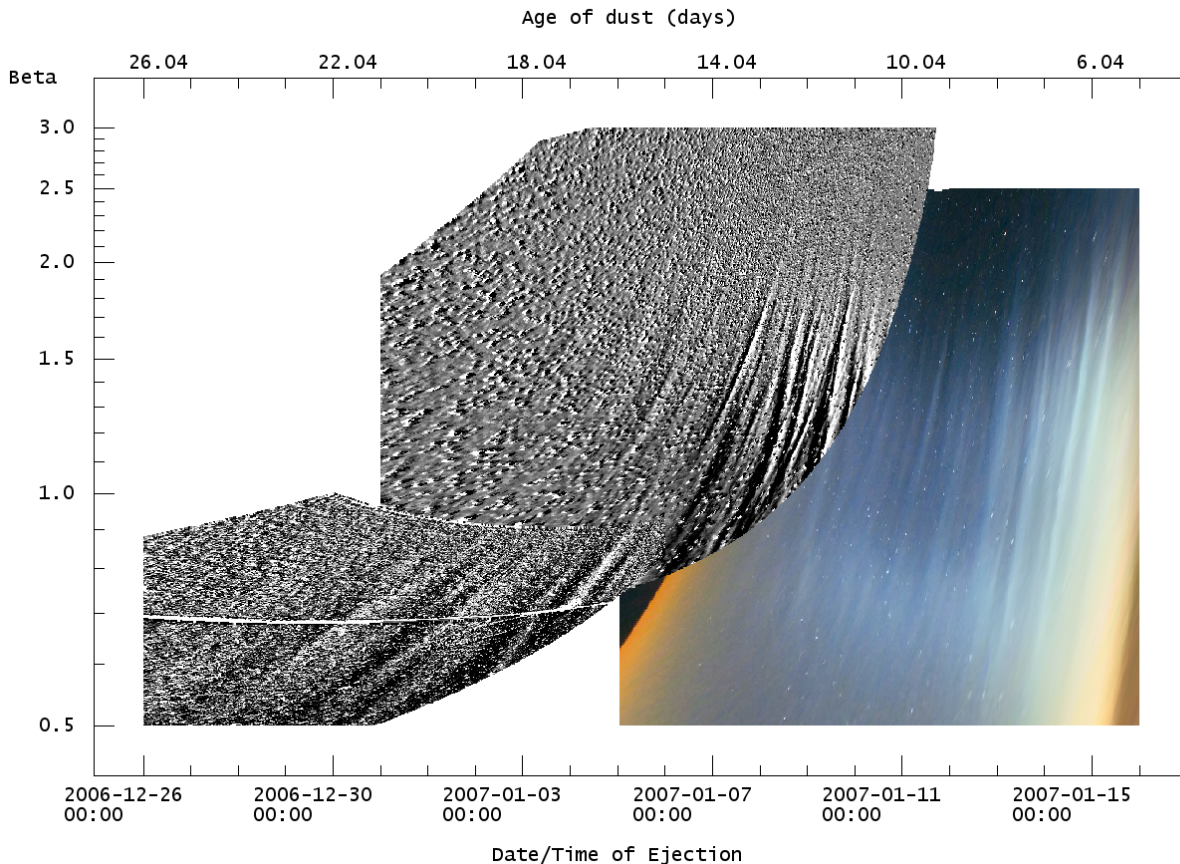


Figure 8: Three week temporal map of the dust tail on January 21 at 01:00 UT, from STEREO HI-1 and HI-2 difference images and from Earth. This is a temporally mapped version of the mosaic shown in Figure 7.

#### 313 4.3. Neutral Iron Tail and Associated Features

314 Another noteworthy feature is the neutral iron tail. This appears as a separate, thin tail at high  $\beta_r$ . Theoretical  
 315 calculations show that neutral iron would have an equivalent  $\beta_r$  of  $\sim 6$ , which provides a reasonable fit to the location  
 316 of the tail (Fulle et al., 2007). Additionally, we note here from difference image from the HI-1 camera that material  
 317 can be seen filling the gap between this iron tail and the main dust tail.

318 The iron tail was visible within both the STEREO-A HI-1 and HI-2 datasets. We created two maps to show this  
 319 higher  $\beta_r$  region including features out to and including the iron tail. A series of 72 temporal maps using difference  
 320 images shows features between  $1 \leq \beta_r \leq 9$ , from 00:00 UT on the 12th January 2007 until 00:00 UT on the 18th  
 321 January. This sequence is available as an animation at the following link:

322 Uploaded Media: [iron\\_tail\\_difference.gif](#)

323 This sequence shows the material between the iron tail and main tail, and a frame from this sequence can be seen in  
 324 Figure 10.

325 Using the STEREO-A HI-1 data with a MGN enhancement, we created another series of 56 temporal maps  
 326 focusing on the iron tail where  $4 \leq \beta_r \leq 9$ , from 2007 January 12 02:00 UT until January 16 20:00 UT. This sequence  
 327 is available as an animation at the following link:

328 [iron\\_tail\\_MGN.gif](#)

329 A frame from this sequence can be seen in Figure 11.

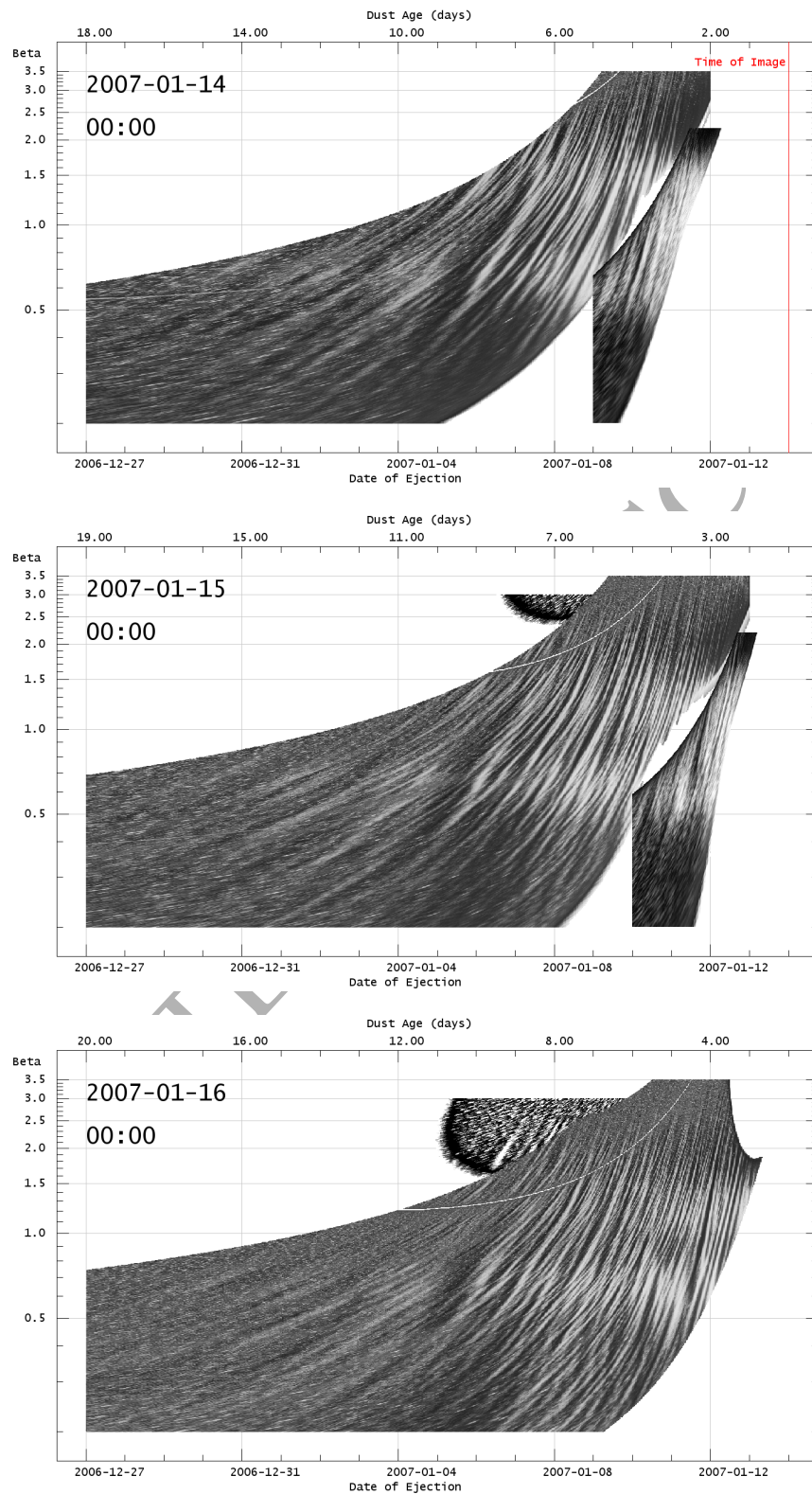


Figure 9: Sequence of three temporal maps based on images taken 24 hours apart, which show the progressive disruption and realignment of the striae in the dust tail.

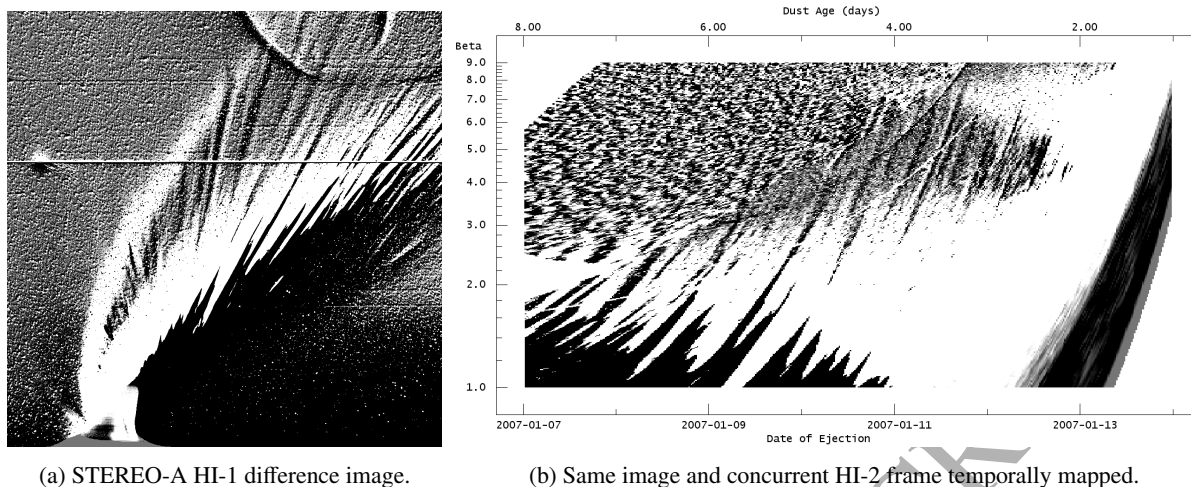


Figure 10: Striae features between the main dust tail and iron tail on January 15 at 12:00 UT, accentuated through the use of the difference image technique. Panel (a) shows an original difference image from SECCHI-HI1. The upper tail is believed to be a neutral iron tail (Fulle et al., 2007). Near-linear features are seen to connect the main dust tail to the inferred iron tail for  $\beta_r=3-7$ . Panel (b) shows the same image presented as a temporal map.

330 The iron tail appears clearly, at high  $\beta_r$ . Our temporal mapping suggests that  $\beta_r \sim 7$  is a closer fit to the position  
 331 and orientation of the iron tail, as opposed to the value of  $\beta_r \sim 6$  given by Fulle et al. (2007). The tail appears to be  
 332 undetectable beyond an age of  $\sim 4.5$  days. However, as the iron tail is a fast moving young feature compared to the  
 333 main tail, it spreads over a large  $\beta_r$  range of 5.5 to 8.5. Additionally, like the main tail, the iron tail was also apparently  
 334 striated. Vertical features in the temporal maps no more than two days old can be seen in these iron tail maps. These  
 335 orientations are compatible with instantaneous release of material from the nucleus.

336 Mapping the region between the iron tail and main tail reveals a band of fainter, higher  $\beta_r$  striae, only visible in  
 337 difference images. These reveal that many of the striae in the main tail extend from where  $\beta_r \sim 1$ , to higher values,  
 338 often reaching  $\beta_r \sim 8$ , i.e. forming features that extend into the main portion of the iron tail.

339 Dust of  $\beta_r$  this high is not reported to be commonly observable (Fulle, 2004), or explainable by traditional theory  
 340 (Burns et al., 1979), although considerations of the relatively recent *in situ* observations of fluffy dust aggregates by  
 341 *Rosetta* instruments (e.g. Bentley et al. 2016) has yet to make its way into radiation pressure theory.

342 We propose several explanations for these features. These striae may form from a Sekanina or Nishioka type  
 343 fragmentation process, which could release iron atoms contained within the parent dust. These atoms would then drift  
 344 anti-sunward with a much higher  $\beta_r$  than observed in a typical striae, but wouldn't reach the iron tail proper, whose  
 345 position is consistent with release from the nucleus, instead filling the gap between.

346 Alternatively, these very high  $\beta_r$  features may represent a continuum of even smaller grains. For very small  
 347 particles approaching the wavelength scales of light, the relative magnitudes of forces for such small grains due to  
 348 radiation pressure are smaller than for larger particles. That is, the effective  $\beta_r$  doesn't increase as rapidly as a function  
 349 of decreasing size and concurrent increase in cross-sectional area:mass ratio. When grains become comparable in size  
 350 to the wavelength of the solar photons impinging on them, radiation pressure becomes ineffective, as does the ability  
 351 of very high  $\beta_r$  grains to scatter light.

#### 352 4.4. Striae Formation

353 Using the SOHO LASCO C3 Blue filter dataset, a sequence of 70 temporal maps was created. These maps cover  
 354 the range  $0.3 \leq \beta_r \leq 2.5$ , from 2007 January 12 20:45 UT until January 15 18:45 UT. This sequence is available as an  
 355 animation at the following link:

356 Uploaded media: formation\_sequence\_linear.gif



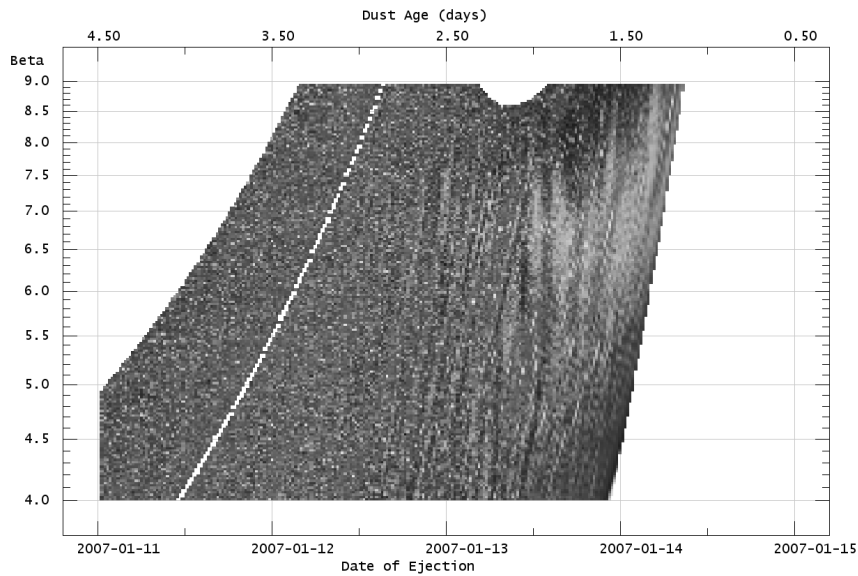


Figure 11: Fine-scale structure in the iron tail as seen from STEREO-A HI-1. The vertical orientation of several January 13 features is consistent with abrupt release from the cometary nucleus on that date.

Striated features are clearly present, however due to the strong brightness gradient across the tail, they are difficult to track. The same sequence is presented again, with a simple unsharp mask applied to each frame by subtracting a Gaussian blurred version of the image. The unsharp masked sequence is available here:

Uploaded media: [formation\\_sequence\\_enhanced.gif](#)

A few frames from both sequences are shown in Figure 12.

Remarkably, this sequence captures the formation of several striae; the authors believe that this is the first time that this process has been captured. From the features for which there are several days' worth of visibility, we explore the characteristics of formation for any clues on which mechanism might provide the best explanation.

Striated features appear to form in the dust approximately 2 to 2.5 days after release from the nucleus, assuming that the Finson-Probst model is correct.

Visually, the striae usually form as juxtaposed regions that both brighten and darken. The smooth tail from which they form displays no sign of any detectable variations in brightness above background gradients. The appearance of features only reveals fully formed striae. We note that striae do not form in strict chronological order according to dust release; more prominent features seem to form from younger dust and may do so before all corresponding older dust has become striated. The observed formation is therefore suggestive of a rearrangement of existing dust, rather than of fragmentation occurring on a specific timescale.

Additionally we note that a particularly large gap forms from dust released up to and around midnight on January 12. This feature forms on the morning of January 14, as seen in Figure 12, and remains notable throughout the LASCO C3 and STEREO-A HI-1 images taken after that time. We refer to this feature henceforth as the *notch*.

In order to understand precisely the role of solar radiation in the formation of these features, an additional mapping technique has been created for this sequence. We follow all the same steps as in section 3.3, the only difference being that instead of plotting with  $t_e$  on the x-axis, we instead align features on this axis along radial sunward lines. To label these features, we refer to the time at which each sunward line would have been crossed by the comet nucleus. This sequence is available here:

Uploaded media: [sunward\\_aligned\\_formation.gif](#)

A frame from this sequence and its original temporal map are shown in figure 13.

Studying the images taken by author M.D., we note that striae apparently continued to form many days after perihelion; figure 14 shows dust released on the January 20 still appears to display striated characteristics.

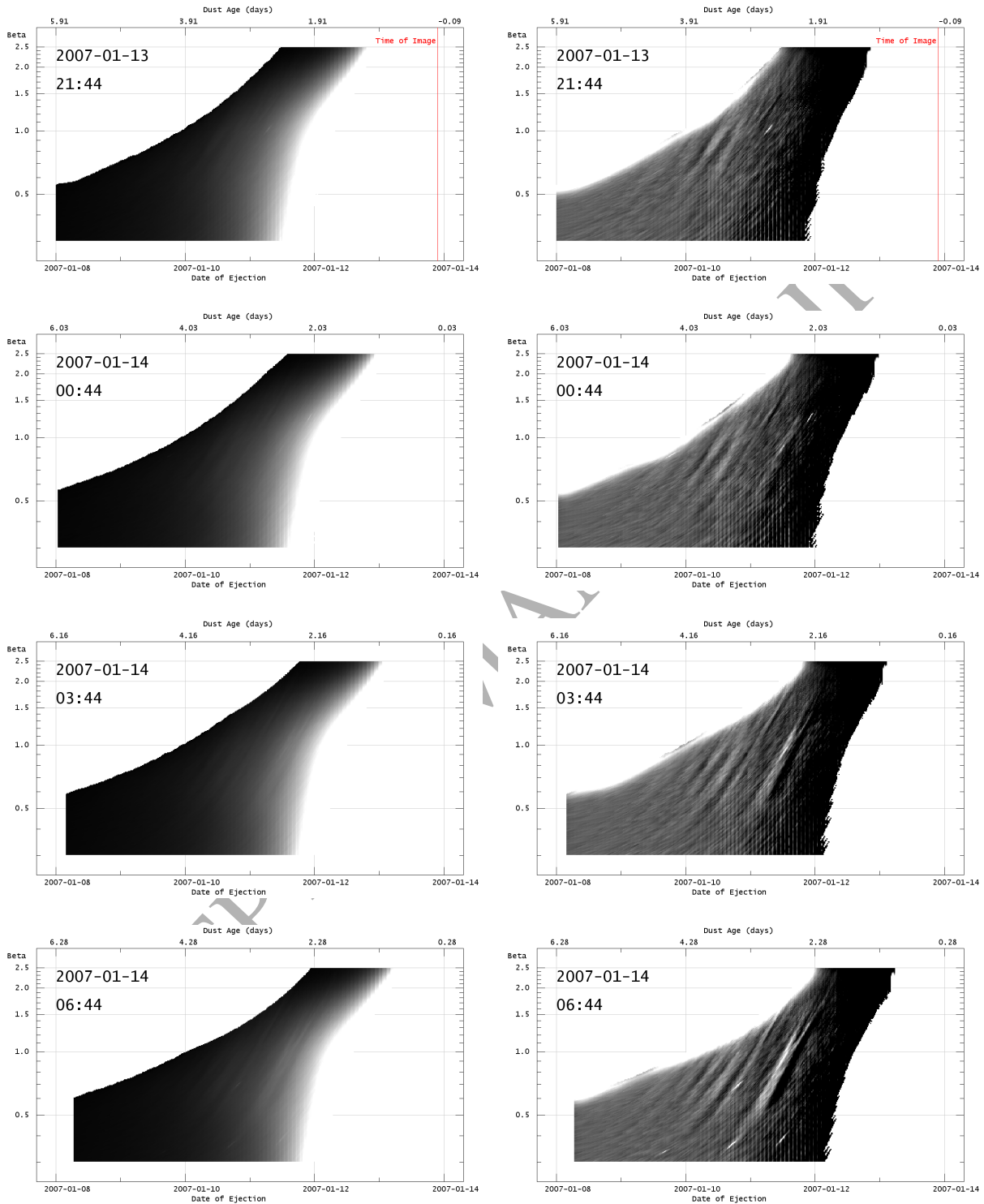


Figure 12: A sequence of four pairs of temporal maps of the younger dust tail as seen in the SOHO LASCO C3 Blue filter datasets. The left images are temporal maps of the raw data, and the right images are the same temporal maps enhanced to show the structure. Across a 9 hour period, structures form from dust released on the 11th January.

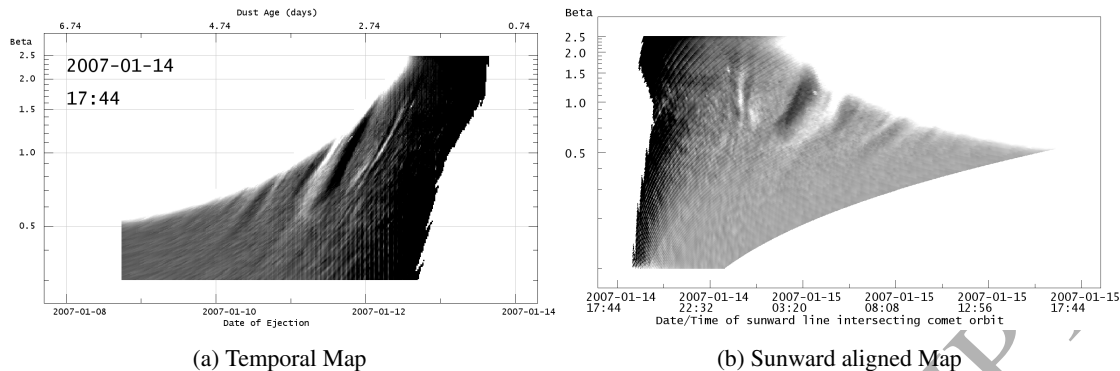


Figure 13: Snapshot of striae formation observed by LASCO C3 with its Blue filter. A narrow stria is visible in the temporal map in panel (a) that has recently formed from dust released early on January 12. Panel (b) shows the same data projected such that each tail section is plotted against the time when the nucleus lay along the radial line from the Sun to the tail section. Features aligned with the local radial sunward direction will therefore appear vertical. The January 12 stria in (a) appears to be perfectly aligned with sunward, as do both of the dark lanes that formed either side of it. Note that time runs from left to right in panel (b), with the youngest tail regions on the left.

#### 4.5. *Striae Disruption and Reorganisation*

Before the temporal mapping was applied to the STEREO-A HI-1 dataset, it was already clear that some process was disrupting the striae. Initially, the striae appeared as straight features as expected, as can be seen in Figure 4. By January 16, many individual striae close to the nucleus had lost their distinct form. The younger tail section appeared more as a loose assortment of apparently *interleaved* striae-like features, shown in Figure 15. The orientation of original striae can be loosely made out, as well as a secondary orientation of the disrupted features, which point roughly sunward.

Figure 16 shows this change in structuring more clearly. In this image, the older striae still maintain their original morphology, however, later on they too become disrupted, and the disruption appears to commence at a fixed region in inertial space. This rearrangement of striae eventually affected all parts of the dust tail observed by SECCHI HI, including the parts further from the Sun only observed by HI-2. This progressive realignment, generally affecting younger dust first, and then the older material, rules out an explanation that the process is due to some kind of temporal dependence of the properties of the emitted dust, as might appear at first. The most likely explanation is therefore some kind of spatially-based one in which a localised phenomenon gradually affects the entire tail.

Before any further analysis can be done, the nature of the disruptive process must be better understood. This is hard to define purely from the original images, in a spatial and temporal sense, due to the transient motion and change in viewing conditions of the tail. We therefore targeted the development of the temporal mapping described here to allow for the precise description of this disruption process.

This is where the temporal map that we have created of the main tail becomes important (Figure 9):

Uploaded Media: `main_striae_evolution_sequence.gif`

As was mentioned, this gives a view of the main dust tail where  $0.2 \leq \beta_r \leq 3$ , which is the affected region. By utilising multiple datasets we can gather a two week picture from 2007 January 11 00:00 UT, before any disruption has occurred, until January 25 02:00 UT, well after the disruption begins, allowing us to see how it permanently affects the tail structure.

From the inspection of this dust temporal map sequence, more conclusions can be drawn about the disruptive process, and the form of the reorganisation process is immediately more clear. The bright stria with  $\beta_r = 1$  for dust released on January 9 in Figure 9 provides a good example. On midnight on January 14 it has just started to be affected, appearing still as a definite feature with some variation. One day later, the disruption has started to occur to the lower  $\beta_r$  dust in the striae, forming some interleaved striae. This takes the form of thin, striated features which appear to transect the pre-existing striae at a different angle. After another day, the stria no longer exists as a continuous structure, instead appearing as a feature comprised of many different sections of interleaved striae.

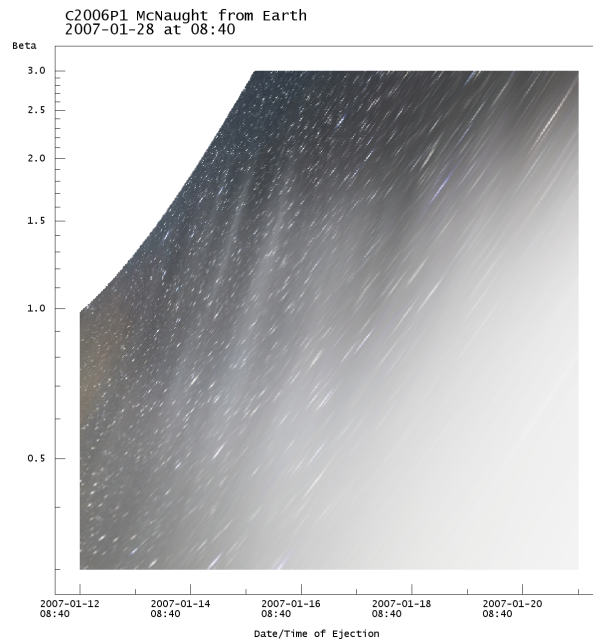


Figure 14: Unenhanced temporal map of image taken in Argentina by author M.D., capturing the last striae observed to form to the authors' knowledge during McNaught's apparition. The "notch" is at the extreme left of this map.

416 Unfortunately there are some limitations of the mapping accuracy at the beginning of the sequence. The slightly  
 417 imperfect astrometric data of the original STEREO-A HI files during instrument commissioning means that features  
 418 on January 11 and 12 move around slightly in the temporal maps. This motion is strictly non physical, and is only  
 419 due to inconsistencies in the FITS metadata during the beginning of the temporal sequence. Additionally, as this dust  
 420 is younger and the tail fills less of the HI-1 field of view, there is a sharpening of features as the tail expands and the  
 421 sampling rate of the mapping improves. Finally there is a six hour data gap between 16:00 and 22:00 on January 12.

422 These effects mean that it is hard to pinpoint the exact time at which reorganisation starts within the striae. At  
 423 best, we can say that global striae reorganisation is first observed definitively on January 13, when the first of the  
 424 interleaved striae are seen. The reorganization appears to begin at a fixed region in inertial space, i.e. consistent with  
 425 a change in the space environment which the comet and its tail are traversing.

#### 426 4.6. Evidence of Solar Wind Effects

427 The most obvious candidate for a cause of the strong localised striae reorganisation is the variation in the solar  
 428 wind conditions at the comet. To investigate the likely solar wind conditions at McNaught, we extracted the modelled  
 429 conditions nearest to the comet's nucleus in the CORHEL inner heliosphere MHD simulation (Odstrcil et al., 2004),  
 430 for Carrington Rotation 2052 (2007 January 8 to February 4). The model run employed solar magnetogram data from  
 431 both SOLIS and the Wilcox Solar Observatory (the latter not shown). Due to its high orbital inclination, McNaught  
 432 was only within the  $\pm 60^\circ$  heliolatitude simulation domain during 2007 January 11 to 19.

433 The global corona is modelled by the Magnetohydrodynamics Around a Sphere (MAS) 3D MHD code (Linker  
 434 et al., 1999; Mikić et al., 1999). Photospheric magnetic field observations provide the boundary conditions, from  
 435 which initial conditions are derived by a potential field solution to the photospheric radial field, a uniform boundary  
 436 density and a Parker-type solar wind outflow. The MAS coronal solution acts as a boundary condition for the he-  
 437 liospheric model, in this case the ENLIL 3D ideal MHD code developed at NOAA/SEC, e.g., Odstrcil (2003), and  
 438 references therein. ENLIL's standard computational domain covers 30 solar radii to 1 AU, and  $-60^\circ$  to  $+60^\circ$  in solar  
 439 latitude. See Odstrcil et al. (2004) and Luhmann et al. (2004) for details of the code coupling. The heliospheric  
 440 solution was allowed to relax to a steady state.



Figure 15: The tail of McNaught on 2007 January 16 at 00:01, as seen from HI-1 on STEREO-A. The nucleus has just left the field of view. At the younger end of the tail the striated form of the tail that was seen earlier (e.g. Figure 4) has been replaced by striae-like features with a more disrupted appearance. The far end of the tail where the features are oldest still maintains its striated structure, although later it too becomes disrupted. The “notch” feature referred to in the text is visible at extreme lower left.

441 The CORHEL results, using SOLIS input data, are presented in Figures 17 and 18. The results based on both  
 442 SOLIS and Wilcox Solar Observatory data (the latter not shown in Figure 17, but qualitatively similar) imply a clear  
 443 change in solar wind conditions centered on early January 13, when the nucleus crossed the heliospheric current sheet,  
 444 HCS, that separates regions of opposite heliospheric magnetic field polarity. McNaught crossed from the northern  
 445 hemisphere’s then inward magnetic polarity to the southern outward polarity. Around the HCS crossing were solar  
 446 wind plasma changes associated with the comet crossing the streamer belt, including a drop in plasma temperature, a  
 447 significant increase in solar wind number density, and a drop in solar wind speed. A second, more modest period of  
 448 varying solar wind conditions was centered on early January 15, visible in Figure 17 as a region of slower solar wind  
 449 associated with a large equatorial active region at Carrington longitude  $\sim 245^\circ$ .

450 The clear correlation between the obvious changes in the striae orientation and the crossing of the HCS by Mc-  
 451 Naught presents, in our opinion, a persuasive case that the dust grains in McNaught’s tail show clear evidence of an  
 452 interaction between the solar wind and comet. The most obvious reason for such an observable change coincident  
 453 with the HCS crossing is the expected large change in the Lorentz force acting on electrically charged particles. The  
 454 Lorentz force is associated with the motional electric field generated by the solar wind flow past the comet. A reversal  
 455 in heliospheric magnetic field direction associated with a HCS crossing would result in a potentially dramatic change  
 456 in direction of the Lorentz force. Electrically charged grains south of the HCS would therefore be accelerated in a  
 457 different direction to that induced by the Lorentz force direction north of the HCS. Such an observable effect associ-  
 458 ated with a HCS crossing was predicted by Horanyi and Mendis (1987), and described more recently by Mendis and  
 459 Horányi (2013).

460 Kramer et al. (2014) inferred an observable effect on charged dust in the tail of C/1996 O1 (Hale-Bopp) when  
 461 at large heliocentric distances. Finding a dust tail at surprisingly large heliocentric distances of 21.6 and 27.2 AU,  
 462 they found the Finson-Probst model alone to be insufficient to explain even the basic orientation of the tail. Out  
 463 of several candidate forces, they found the Lorentz force the best explanation for the shape, inferring its importance  
 464 to dust dynamics at high heliocentric distances. This is due to the Lorentz force having only a  $r^{-1}$  dependence with  
 465 heliocentric distance. Whilst we are dealing here with small heliocentric distances, the result that the dust is charged  
 466 strongly enough for its motion to be affected is important.

467 We regard a comprehensive study of the changing solar wind effects on the comet as being outside the scope of  
 468 this paper, and we therefore defer such a study to a later publication. Several complicating factors in understanding  
 469 the nature of the dust-solar wind interactions include the fact that the estimated solar wind conditions that we can  
 470 easily derive are those for the comet's head only, whereas the striae which are observed to change in orientation are up  
 471 to 0.4 AU further away from the Sun. We also note that the HCS is distorted at a comet's head due to magnetic field  
 472 line-draping; dust particles in the coma in particular will therefore have likely encountered a complex magnetic field  
 473 structure, not a relatively simple reversal of magnetic field direction. In addition, as local undulations in the HCS may  
 474 exist, and as the line of intersection between the comet's orbit and the HCS is gradually changing with the rotation of  
 475 the sun and the propagation of solar wind structures, the exact locations in inertial space where the Lorentz force is  
 476 modified in the tail may be changing with time.

477 It is possible to estimate the comparative magnitude of a Lorentz force to radiation pressure and gravity. At an  
 478 average position in the tail at a heliocentric distance of 0.25 AU, this is roughly:

$$a_{FP} = \frac{(1 - \beta_r)GM_\odot}{r^2} \approx (1 - \beta_r)0.1ms^{-2} \quad (4)$$

479 The Lorentz force can be formulated as:

$$\vec{a}_{Lorentz} = \frac{q}{m} [(\vec{v}_{dust} - \vec{v}_{sw}) \times \vec{B}] \quad (5)$$

480 The solar wind speed  $\vec{v}_{sw}$  dominates above the dust speed  $\vec{v}_{dust}$  and so the azimuthal component of the magnetic  
 481 field is the most important component. The charge to mass ratio can be related to  $\beta_r$  (Kramer et al., 2014):

$$\frac{q}{m} = \frac{12\varepsilon_0 V}{C^2} \beta_r^2 \frac{\rho_d}{Q_{pr}} \quad (6)$$

482 Allowing for an estimate of the magnitude of the Lorentz force to be made:

$$a_{Lorentz} = \frac{12\varepsilon_0 V}{C^2} \beta_r^2 \frac{\rho_d}{Q_{pr}} B_\phi v_{sw} \quad (7)$$

483 Assuming dust is charged to +5V, with  $\rho_d = 1000kgm^{-3}$  and  $Q_{pr} = 1$ , taking the values of  $B_\phi = 10nT$  and  
 484  $v_{sw} = 300kms^{-1}$  from figure 18, and using the constant  $C = 5.76 \times 10^{-4}kgm^{-2}$ , we can obtain a guess for the  
 485 magnitude of the Lorentz force as:

$$a_{Lorentz} = \beta_r^2 0.005ms^{-2} \quad (8)$$

486 Hence, assuming a continuous Lorentz force acting on the dust when the comet was still north of the current  
 487 sheet and associated streamer belt, at the HCS crossing where we see a change from  $B_\phi$  from 10 nT to -10 nT, the  
 488 orientation change of the Lorentz force may account for a sudden perturbation in the motion of the dust. This could  
 489 be at least 10% the magnitude of gravity and radiation pressure, and higher for high  $\beta_r$  dust, which is easily enough to  
 490 affect the dynamics of the dust. The implication that the Lorentz force clearly has observable effects – that may only  
 491 become readily apparent when the strength and/or direction of that force changes – should be included in any future  
 492 comprehensive studies of cometary dust dynamics. We note that Kimura et al. (1985) concluded that the behaviour  
 493 of striae in C/1957 P1 (Mrkos) and C/1975 V1 (West) implied the presence of nonradial perturbations which they  
 494 concluded were most likely Lorentz forces, with a more general discussion of solar wind effects on dust at comets  
 495 being also discussed around that time by Ip et al. (1985).

496 The implications of the Lorentz force's observable effects include a complication in the interpretation of striae.  
 497 Once the comet crossed the current sheet, there were three "families" of dust present in the tail:

- 498 1. those released prior to crossing the HCS, and still north of the HCS, and unperturbed by any change in the  
 499 motional electric field
- 500 2. those released prior to crossing the HCS, but had subsequently crossed the HCS during which time their dy-  
 501 namical behaviour has been altered
- 502 3. those released after HCS crossing, in a "new" near-steady magnetic field regime, and hence unaffected by  
 503 changes during the HCS crossing itself

A careful future study of the relative behaviour of these three families of particles could provide useful constraints on the magnitude of the forces involved, and could in turn improve our understanding of the relationship between the inherent  $\beta_r$  value of dust grains, their actual masses, and their cross-sectional area to radiation pressure.

In future studies of these effects, it should also be borne in mind that changes in the dynamic pressure of the solar wind may also be detectable, e.g. Gustafson (1994); Minato et al. (2004), especially when reasonably close to the Sun where the solar wind number density is relatively high. We note that the formation of the prominent “notch” feature so close to the time when the nucleus was apparently crossings the HCS may be related to the then-rapidly changing solar wind conditions at the comet’s head.

#### 4.7. Striae Lifetime

The extended observational dataset used here allows individual striae to be tracked for longer than in previous studies that were based on much smaller ground based datasets. This enabled us to study the longevity of the striae; in particular using the STEREO-A HI-1 and HI-2 datasets, and also loosely relate the dependence of these lifetimes on  $\beta$ .

Striae remain visible in both maps when studying difference images, although the signal to noise ratio at times is extremely poor due to the noise associated with the moving background starfield. A statistical extraction of the signal is therefore difficult and we are therefore reliant on the somewhat flawed method of visual inspection. In particular we run into two observational biases: we *expect* to see features and may be convinced that we can see some after they may have actually disappeared, and we may have a heightened ability to see *moving* features.

This leads to a discrepancy between methods of study. Looking at individual temporal mapped frames, striated features in STEREO-A HI-1 data remain just visible until around midday on January 22, and those in HI-2 can be seen until midday on the 27th. Looking however at an animation of the original difference enhanced FITS images, the relative motion of the striae actually allows our eyes to continue to perceive the presence features for a few extra days, in HI-1 until January 24 and HI-2 until the 30th.

The temporal maps do allow for the original release times of the released striae material and their  $\beta$  ranges to be read off easily and these can be cross referenced with the original images to work out which are the longest surviving striae. The oldest HI-1 features are at  $0.5 \leq \beta \leq 0.8$  and date back to midday on 2006 December 29, meaning the oldest features are just over 26 days old. In HI-2, the longest lasting striated features are at  $1.2 \leq \beta \leq 1.8$  and were formed on January 7 to 8, making them 23 days old. These two samples roughly represent the two peaks of the bimodal dust distribution.

For the material within the iron tail, lifetimes are much shorter than in the main dust tail, with features disappearing from temporal maps within 5 days. If this material is indeed composed of iron atoms, then this is controlled by the atoms’ photoionization lifetime, as studied by (Fulle et al., 2007). If grains exist in this tail, then this inverse relation of apparent lifetime to  $\beta$  may be mainly due to higher  $\beta$  features spreading out more quickly and reducing in surface brightness faster than the main dust tail. There may also be some dependence on increased fragmentation and destruction by sublimation of smaller grain sizes.

## 5. Conclusions and Discussion

### 5.1. The Temporal Mapping Technique

The temporal mapping technique, published here for the first time, has proven itself to be a very useful method for the direct analysis of cometary dust tails. It allows for effects of physical scale, transient motion and observer geometry to be removed, and has enabled us to combine and investigate numerous images of McNaught from different sources. This co-mapping has proven to be very successful, with tail features remaining steady at the fixed formation age- $\beta$ , location in phase space. The authors plan to apply this analysis method to other comets in the future.

### 5.2. Dust-Solar Wind Interactions

The McNaught observations confirm that solar wind conditions can have a significant effect on observable dust tail structure. We believe that the most likely cause of the observed effects are due to changes in the Lorentz force, as previously predicted (Horanyi and Mendis, 1987). One puzzling aspect of the striae rearrangement associated with the HCS crossing is that the effect is observable at all. It has been known for many years that charged dust grains’

551 trajectories can be affected by Lorentz forces, but these have only been observed previously by *in situ* observations in  
 552 various solar system contexts, e.g. Strub et al. (2015); Hsu et al. (2011), and these populations have been generally  
 553 regarded as being too small for remote observation in the visible range.

554 For example, studies of Jupiter's gossamer ring particles with the *Galileo* spacecraft dust detector revealed the  
 555 presence of high inclination grains down to  $\sim 0.3 \mu\text{m}$  in scale that were not visible in images of the same ring (Hamilton  
 556 and Krüger, 2008), where particles only a few  $\mu\text{m}$  across and larger were detectable. The observations presented here,  
 557 together with those of Kramer et al. (2014), imply that grains strongly susceptible to electrodynamic forces are larger  
 558 than had been previously anticipated. The authors plan to make quantitative estimates of the masses and effective  
 559 areas of these grains as part of a future study.

### 560 5.3. Striae Formation

561 Assuming that our interpretation of the solar wind interaction is correct, some aspects of the observed changes in  
 562 the striae on crossing the HCS can help provide constraints on the proposed striae formation processes.

563 If the Sekanina and Farrell (1980) two-step formation process is responsible for striae, then each stria would  
 564 contain a progressively higher  $\beta_r$  with increasing distance from the Sun, hence the regions of striae farthest from the  
 565 Sun would exclusively contain the highest  $\beta_r$  (generally lowest mass) grains. In this situation, the furthest extremities  
 566 of the striae would therefore be most susceptible to the Lorentz force, and to changes to it, hence to a HCS crossing.

567 If instead the Nishioka (1998) "cascade" striae formation process is operating, each stria would contain a more  
 568 homogeneous distribution of  $\beta_r$  values along its length, as a result of multiple fragmentation events leading to the  
 569 formation of each linear structure. Crossing the HCS with this  $\beta_r$  distribution would lead us to expect disruption to  
 570 occur throughout the length of a stria on the reversal in polarity of the heliospheric magnetic field, and hence a change  
 571 in the Lorentz force direction.

572 The appearance of "interleaved" striae after the HCS crossings is certainly in better agreement with the latter  
 573 scenario, with multiple regions along each stria showing a displaced portion. Our analysis strongly suggests that  
 574 Nishioka's "cascade" model best fits the observations, and that striae are not formed in single fragmentation events,  
 575 at least for Comet McNaught.

576 The mechanism detailed by Froehlich and Notni (1988) also explicitly considers the co-existence of multiple  $\beta_r$   
 577 dust along the striae due to optical thickness effects. They claim that higher relative  $\beta_r$  particles may exist on one  
 578 side a cloud furthest from the sun, with lower  $\beta_r$  particles existing on the near side. Although Steckloff and Jacobson  
 579 (2016) do not make any such definitive statements, we note that due to the cascading formation of striae it should  
 580 allow for these "interleaved" striae to be present.

581 We again note the remarkable sequence of stria formation recorded by LASCO and presented in section 4.4. Each  
 582 stria appears to essentially form as a largely complete region which suddenly brightens over 6-9 hours. If a Sekanina  
 583 or Nishioka type formation process was occurring, the striae would form from parent particles of a small range of  $\beta_r$ ,  
 584 and would then spread out as the daughter particles distinguished themselves by their characteristic  $\beta_r$ . There is little  
 585 observational evidence to suggest a mechanism where they extend in  $\beta_r$  as time progresses, except perhaps at the high  
 586 and low  $\beta_r$  ends of the striae.

587 Some striae appear to form almost perfectly aligned with the radial direction from the sun, a good example high-  
 588 lighted earlier in figure 13. Many such striae also form in conjunction with dark lanes adjacent to the striae, giving the  
 589 appearance of material being swept together to form striae. These effects are both consistent with, and appear to hint  
 590 towards the role of optical thickness and shadowing mechanisms having importance in the formation of some striae,  
 591 as detailed in Froehlich and Notni (1988).

592 Striae do not form chronologically with dust ejection time. This is quite well explained by the high variability in  
 593 the "Sublimation-YORP", or SYORP, timescales proposed in the work of Steckloff and Jacobson (2016), although it  
 594 is not strictly forbidden by any of the other mechanisms.

595 As the directly-observed stria formation took place during January 15, when from the CORHEL model we expect  
 596 that the comet was undergoing changes in its solar wind environment, we tentatively speculate that those particular  
 597 striae may be formed through a change in the comet's solar wind conditions, rather than through a fragmentation-only  
 598 process that may be responsible for many, if not most, of these spectacular structures.



## 6. Acknowledgements

OP is supported by a UK Science and Technology Facilities Council (STFC) PhD studentship. GHJ is grateful to STFC for partial support through consolidated grants ST/K000977/1 and ST/N000722/1. KB is supported by the NASA-Funded Sungrazer Project. *Astrometry.net* is funded by the US National Science Foundation, the US National Aeronautics and Space Administration, and the Canadian National Science and Engineering Research Council. The SOHO/LASCO data used here are produced by a consortium of the Naval Research Laboratory (USA), Max-Planck-Institut für Sonnensystemforschung (Germany), Laboratoire d'Astronomie (France), and the University of Birmingham (UK), and are available via <https://sohowww.nascom.nasa.gov/data/>. SOHO is a project of international cooperation between ESA and NASA. The STEREO/SECCHI data are produced by an international consortium of the NRL (USA), LMSAL (USA), NASA-GSFC (USA), RAL (UK), University of Birmingham (UK), MPS (Germany), CSL (Belgium), IOTA (France), and IAS (France), and are available via <https://stereo-ssc.nascom.nasa.gov/>. SOLIS magnetograms are produced cooperatively by NSF/NSO and NASA/LWS. The National Solar Observatory (NSO) is operated by the Association of Universities for Research in Astronomy, Inc., under cooperative agreement with the National Science Foundation. This research made use of Astropy, a community-developed core Python package for Astronomy (Astropy Collaboration, 2013).

## References

- Astropy Collaboration, 2013. Astropy: A community python package for astronomy. *Astronomy & Astrophysics* 558, A33.
- Battams, K., Knight, M. M., may 2017. SOHO comets: 20 years and 3000 objects later. *Philosophical Transactions of the Royal Society A: Mathematical, Physical and Engineering Sciences* 375 (2097), 20160257.
- Bentley, M. S., Schmied, R., Mannel, T., Torkar, K., Jeszenszky, H., Romstedt, J., Levasseur-Regourd, A.-C., Weber, I., Jessberger, E. K., Ehrenfreund, P., Koeberl, C., Havnes, O., 2016. Aggregate dust particles at comet 67P/ChuryumovGerasimenko. *Nature* 537 (7618), 73–75.
- Bewsher, D., Brown, D. S., Eyles, C. J., Kellett, B. J., White, G. J., Swinyard, B., jun 2010. Determination of the photometric calibration and large-scale flatfield of the STEREO heliospheric imagers: I. HI-1. *Solar Physics* 264 (2), 433–460.
- Brueckner, G., Howard, R., Koomen, M., Korendyke, C., Michels, D., Moses, J., Socker, D., Dere, K., Lamy, P., Llebaria, A., et al., 1995. The large angle spectroscopic coronagraph (lasco). *Solar Physics* 162 (1-2), 357–402.
- Burns, J. A., Lamy, P. L., Soter, S., oct 1979. Radiation forces on small particles in the solar system. *Icarus* 40 (1), 1–48.
- Combi, M. R., Boyd, Z., Lee, Y., Patel, T. S., Bertaux, J.-L., Quémerais, E., Mäkinen, J. T. T., Dec. 2011. SOHO/SWAN observations of comets with small perihelia: C/2002 V1 (NEAT), C/2002 X5 (Kudo-Fujikawa), 2006 P1 (McNaught) and 96P/Machholz 1. *Icarus* 216, 449–461.
- Eyles, C., Harrison, R., Davis, C., Waltham, N., Shaughnessy, B., Mapson-Menard, H., Bewsher, D., Crothers, S., Davies, J., Simnett, G., et al., 2009. The heliospheric imagers onboard the stereo mission. *Solar Physics* 254 (2), 387–445.
- Finson, M., Probst, R., 1968. A theory of dust comets. I. Model and equations. *The Astrophysical Journal* 154, 327–380.
- Froehlich, H.-E., Notni, P., 1988. Radiation pressure: a stabilizing agent of dust clouds in comets? *Astronomische Nachrichten: A Journal on all Fields of Astronomy* 309 (2), 147–155.
- Fulle, M., 2004. Motion of cometary dust. pp. 565–575.
- Fulle, M., Leblanc, F., Harrison, R. A., Davis, C. J., Eyles, C. J., Halain, J. P., Howard, R. A., Bockelée-Morvan, D., Cremonese, G., Scarmato, T., May 2007. Discovery of the Atomic Iron Tail of Comet MCNaught Using the Heliospheric Imager on STEREO. *The Astrophysical Journal Letters* 661, L93–L96.
- Giorgini, J. D., Yeomans, D. K., Chamberlin, A. B., Chodas, P. W., Jacobson, R. A., Keesey, M. S., Lieske, J. H., Ostro, S. J., Standish, E. M., Wimberly, R. N., Sep. 1997. JPL's On-Line Solar System Ephemeris and Data Service. In: Bietenholz, M. F., Bartel, N., Rupen, M. P., Beasley, A. J., Graham, D. A., Altunin, V. I., Venturi, T., Umaga, G., Conway, J. E. (Eds.), *Bulletin of the American Astronomical Society*. Vol. 29 of *Bulletin of the American Astronomical Society*. p. 1099.
- Gustafson, B. A. S., 1994. Physics of Zodiacal Dust. *Annual Review of Earth and Planetary Sciences* 22, 553–595.
- Hamilton, D. P., Krüger, H., may 2008. The sculpting of jupiter's gossamer rings by its shadow. *Nature* 453 (7191), 72–75.
- Hilchenbach, M., Kissel, J., Langevin, Y., Briois, C., von Hoerner, H., Koch, A., Schulz, R., Silén, J., Altwegg, K., Colangeli, L., Cottin, H., Engrand, C., Fischer, H., Glasmachers, A., Grün, E., Haerendel, G., Henkel, H., Höfner, H., Hornung, K., Jessberger, E. K., Lehto, H., Lehto, K., Raulin, F., Le Roy, L., Rynö, J., Steiger, W., Stephan, T., Thirkell, L., Thomas, R., Torkar, K., Varmuza, K., Wanczek, K.-P., Altobelli, N., Baklouti, D., Bardin, A., Fray, N., Krüger, H., Ligier, N., Lin, Z., Martin, P., Merouane, S., Orthous-Daunay, F. R., Paquette, J., Revillet, C., Siljeström, S., Stenzel, O., Zaprudin, B., Jan. 2016. Comet 67P/Churyumov-Gerasimenko: Close-up on Dust Particle Fragments. *The Astrophysical Journal Letters* 816, L32.
- Hill, J. R., Mendis, D. A., Nov. 1980. On the origin of striae in cometary dust tails. *The Astrophysical Journal* 242, 395–401.
- Horanyi, M., Mendis, D. A., Jan. 1987. The effect of a sector boundary crossing on the cometary dust tail. *Earth Moon and Planets* 37, 71–77.
- Howard, R. A., Moses, J. D., Vourlidas, A., Newmark, J. S., Socker, D. G., Plunkett, S. P., Korendyke, C. M., Cook, J. W., Hurley, A., Davila, J. M., Thompson, W. T., St Cyr, O. C., Mentzell, E., Mehalick, K., Lemen, J. R., Wuelsel, J. P., Duncan, D. W., Tarbell, T. D., Wolfson, C. J., Moore, A., Harrison, R. A., Waltham, N. R., Lang, J., Davis, C. J., Eyles, C. J., Mapson-Menard, H., Simnett, G. M., Halain, J. P., Defise, J. M., Mazy, E., Rochus, P., Mercier, R., Ravet, M. F., Delmotte, F., Auchere, F., Delaboudiniere, J. P., Bothmer, V., Deutsch, W., Wang, D., Rich, N., Cooper, S., Stephens, V., Maahs, G., Baugh, R., McMullin, D., Carter, T., Apr. 2008. Sun Earth Connection Coronal and Heliospheric Investigation (SECCHI). *Space Science Reviews* 136, 67–115.

- 656 Hsu, H.-W., Kempf, S., Postberg, F., Trieloff, M., Burton, M., Roy, M., Moragas-Klostermeyer, G., Srama, R., Aug. 2011. Cassini dust stream  
657 particle measurements during the first three orbits at Saturn. *Journal of Geophysical Research (Space Physics)* 116, A08213.
- 658 Ip, W.-H., Kimura, H., Liu, C.-P., 1985. Interaction of the cometary dust with the solar wind and cometary plasma. In: Giese, R. H., Lamy, P.  
659 (Eds.), *IAU Colloq. 85: Properties and Interactions of Interplanetary Dust*. Vol. 119 of *Astrophysics and Space Science Library*. pp. 325–328.
- 660 Jones, G. H., Knight, M. M., Battams, K., Boice, D. C., Brown, J., Giordano, S., Raymond, J., Snodgrass, C., Steckloff, J. K., Weissman, P.,  
661 Fitzsimmons, A., Lisse, C., Opitom, C., Birkett, K. S., Bzowski, M., Decock, A., Mann, I., Ramanjooloo, Y., McCauley, P., feb 2018. *The*  
662 *Science of Sungrazers, Sunskirters, and Other Near-Sun Comets*. *Space Science Reviews* 214 (1), 20.
- 663 Karim, A. I. A., 1966. Stability of the fourth order runge-kutta method for the solution of systems of differential equations. *The Computer Journal*  
664 9 (3), 308–311.
- 665 Kelley, M. S., Woodward, C. E., Harker, D. E., Wooden, D. H., Reach, W. T., Fernández, Y. R., Mar. 2010. Comet Dust Diversity in Ground-based  
666 and Spitzer Space Telescope Mid-Infrared Spectra. In: *Lunar and Planetary Science Conference*. Vol. 41 of *Lunar and Planetary Inst. Technical*  
667 *Report*. p. 2375.
- 668 Kharchuk, S. V., Korsun, P. P., Dec. 2010. Striated features in the dust tail of comet C/2006 P1 (McNaught). *Kinematics and Physics of Celestial*  
669 *Bodies* 26, 322–325.
- 670 Kimura, H., Liu, C.-P., Jockers, K., 1985. On the dynamic behavior of dust striae observed in comets West 1976 VI, and MRKOS 1957 V. In:  
671 Giese, R. H., Lamy, P. (Eds.), *IAU Colloq. 85: Properties and Interactions of Interplanetary Dust*. Vol. 119 of *Astrophysics and Space Science*  
672 *Library*. pp. 283–286.
- 673 Koutchmy, S., Lamy, P., Jun 1978. Propagating inhomogeneities in the dust tail of comet west 1975. *Nature* 273 (5663), 522–524.
- 674 Kramer, E. A., Fernandez, Y. R., Lisse, C. M., Kelley, M. S., Woodney, L. M., Jul 2014. A dynamical analysis of the dust tail of comet c/1995 o1  
675 (hale-bopp) at high heliocentric distances. *Icarus* 236, 136–145.
- 676 Kronk, G., 1999. *Cometography: Volume 1, Ancient-1799: A Catalog of Comets*. *Cometography Series*. Cambridge University Press.  
677 URL <https://books.google.co.uk/books?id=Umxbb68tmZMC>
- 678 Lamy, P. L., Koutchmy, S., Feb. 1979. Comet West 1975n. II - Study of the striated tail. *Astron. & Astrophys.* 72, 50–54.
- 679 Lang, D., Hogg, D. W., Mierle, K., Blanton, M., Roweis, S., 2010. Astrometry. net: Blind astrometric calibration of arbitrary astronomical images.  
680 *The Astronomical Journal* 139 (5), 1782.
- 681 Leblanc, F., Fulle, M., López Ariste, A., Cremonese, G., Doressoundiram, A., Sainz Dalda, A., Gelly, B., Apr. 2008. Comet McNaught C/2006 P1:  
682 observation of the sodium emission by the solar telescope THEMIS. *Astron. Astrophys.* 482, 293–298.
- 683 Linker, J. A., Mikić, Z., Biesecker, D. A., Forsyth, R. J., Gibson, S. E., Lazarus, A. J., Lecinski, A., Riley, P., Szabo, A., Thompson, B. J., May  
684 1999. Magnetohydrodynamic modeling of the solar corona during Whole Sun Month. *Journal of Geophysical Research* 104, 9809–9830.
- 685 Luhmann, J. G., Solomon, S. C., Linker, J. A., Lyon, J. G., Mikic, Z., Odstrčil, D., Wang, W., Wiltberger, M., Oct. 2004. Coupled model simulation  
686 of a Sun-to-Earth space weather event. *Journal of Atmospheric and Solar-Terrestrial Physics* 66, 1243–1256.
- 687 Marsden, B. G., Jan. 2007. Comet C/2006 P1 (McNaught). *IAU Circular* 8801.
- 688 Marsden, B. G., Jan. 2007. Comet c/2006 p1 (mcnaught). *International Astronomical Union Circulars* 8796.
- 689 McClure, A., May 1962. Latest Pictures of Comet Seki-Lines. *Sky & Telescope* 23.
- 690 McNaught, R., 2006. Comet c/2006 p1. *International Astronomical Union Circular* 8737, 1.
- 691 Mendis, D., Horányi, M., jan 2013. Dusty plasma effects in comets: Expectations for rosetta. *Reviews of Geophysics* 51 (1), 53–75.
- 692 Mikić, Z., Linker, J. A., Schnack, D. D., Lionello, R., Tarditi, A., May 1999. Magnetohydrodynamic modeling of the global solar corona. *Physics*  
693 *of Plasmas* 6, 2217–2224.
- 694 Minato, T., Köhler, M., Kimura, H., Mann, I., Yamamoto, T., aug 2004. Momentum transfer to interplanetary dust from the solar wind. *Astronomy*  
695 *& Astrophysics* 424 (2), L13–L16.
- 696 Morgan, H., Druckmüller, M., apr 2014. Multi-scale gaussian normalization for solar image processing. *Solar Physics* 289 (8), 2945–2955.
- 697 Morrill, J. S., Korendyke, C. M., Brueckner, G. E., Giovane, F., Howard, R. A., Koomen, M., Moses, D., Plunkett, S. P., Vourlidis, A., Esfandiari,  
698 E., Rich, N., Wang, D., Thernisien, A. F., Lamy, P., Llebaria, A., Biesecker, D., Michels, D., Gong, Q., Andrews, M., feb 2006. Calibration of  
699 the soho/lasco c3 white light coronagraph. *Solar Physics* 233 (2), 331–372.
- 700 Nishioka, K., 1998. Finite lifetime fragment model 2 for synchronic band formation in dust tails of comets. *Icarus* 134 (1), 24–34.
- 701 Nishioka, K., Saito, K., Watanabe, J.-I., Ozeki, T., 1992. Photographic observations of the synchronic band in the tail of Comet West 1976 VI.  
702 *Publications of the National Astronomical Observatory of Japan* 2, 601–621.
- 703 Nishioka, K., Watanabe, J.-I., 1990. Finite lifetime fragment model for synchronic band formation in dust tails of comets. *Icarus* 87 (2), 403–411.
- 704 Notni, P., Thäenert, W., 1988. The striae in the dust tails of great comets - A comparison to various theories. *Astronomische Nachrichten* 309,  
705 133–146.
- 706 Odstrčil, D., Aug. 2003. Modeling 3-D solar wind structure. *Advances in Space Research* 32, 497–506.
- 707 Odstrčil, D., Pizzo, V. J., Linker, J. A., Riley, P., Lionello, R., Mikic, Z., oct 2004. Initial coupling of coronal and heliospheric numerical magneto-  
708 hydrodynamic codes. *Journal of Atmospheric and Solar-Terrestrial Physics* 66 (15-16), 1311–1320.
- 709 Pittichová, J., Sekanina, Z., Birkle, K., Boehnhardt, H., Engels, D., Keller, P., 1997. An Early Investigation Of The Striated Tail Of Comet Hale-  
710 Bopp (C/1995 O1). *Earth, Moon, and Planets* 78 (1/3), 329–338.
- 711 Schulz, R., Hilchenbach, M., Langevin, Y., Kissel, J., Silen, J., Briois, C., Engrand, C., Hornung, K., Baklouti, D., Bardyn, A., Cottin, H., Fischer,  
712 H., Fray, N., Godard, M., Lehto, H., Roy, L. L., Merouane, S., Orthous-Daunay, F.-R., Paquette, J., Rynö, J., Siljeström, S., Stenzel, O.,  
713 Thirkell, L., Varmuza, K., Zaprudin, B., jan 2015. Comet 67p/churyumov-gerasimenko sheds dust coat accumulated over the past four years.  
714 *Nature* 518 (7538), 216–218.
- 715 Sekanina, Z., Farrell, J., 1980. The striated dust tail of comet west 1976 vi as a particle fragmentation phenomenon. *The Astronomical Journal* 85,  
716 1538–1554.
- 717 Sekanina, Z., Farrell, J. A., 1982. Two dust populations of particle fragments in the striated tail of comet Mrkos 1957 V. *Astronomical Journal*  
718 87 (12), 1836.
- 719 Sekanina, Z., Pittichová, J., 1997. Distribution law for particle fragmentation times in a theory for striated tails of dust comets: application to comet  
720 hale-bopp (c/1995 o1). *Earth, Moon, and Planets* 78 (1-3), 339–346.

- 721 Steckloff, J. K., Jacobson, S. A., 2016. The formation of striae within cometary dust tails by a sublimation-driven yorp-like effect. *Icarus* 264,  
722 160–171.
- 723 Strub, P., Krüger, H., Sterken, V. J., Oct. 2015. Sixteen Years of Ulysses Interstellar Dust Measurements in the Solar System. II. Fluctuations in the  
724 Dust Flow from the Data. *The Astrophysical Journal* 812, 140.
- 725 Tappin, S. J., Eyles, C. J., Davies, J. A., Jul 2015. Determination of the photometric calibration and large-scale flatfield of the STEREO heliospheric  
726 imagers: II. HI-2. *Solar Physics* 290 (7), 2143–2170.
- 727 Wooden, D., De Buizer, J., Kelley, M., Sitko, M., Woodward, C., Harker, D., Reach, W., Russell, R., Kim, D., Yanamadra-Fisher, P., Lisse, C., de  
728 Pater, I., Gehrz, R., Kolokolova, L., Jul. 2014. Comet C/2012 S1 (ISON)'s carbon-rich and micron-size-dominated coma dust. In: Muinonen,  
729 K., Penttilä, A., Granvik, M., Virkki, A., Fedorets, G., Wilkman, O., Kohout, T. (Eds.), *Asteroids, Comets, Meteors 2014*.

ACCEPTED MANUSCRIPT

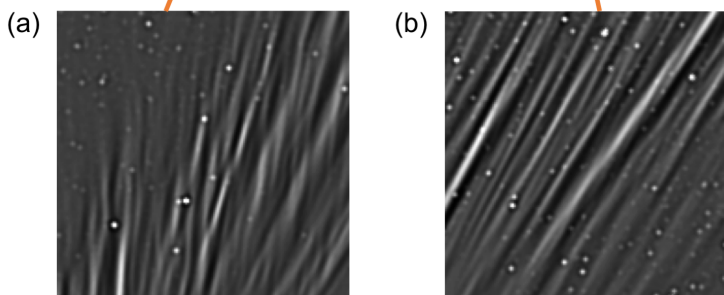
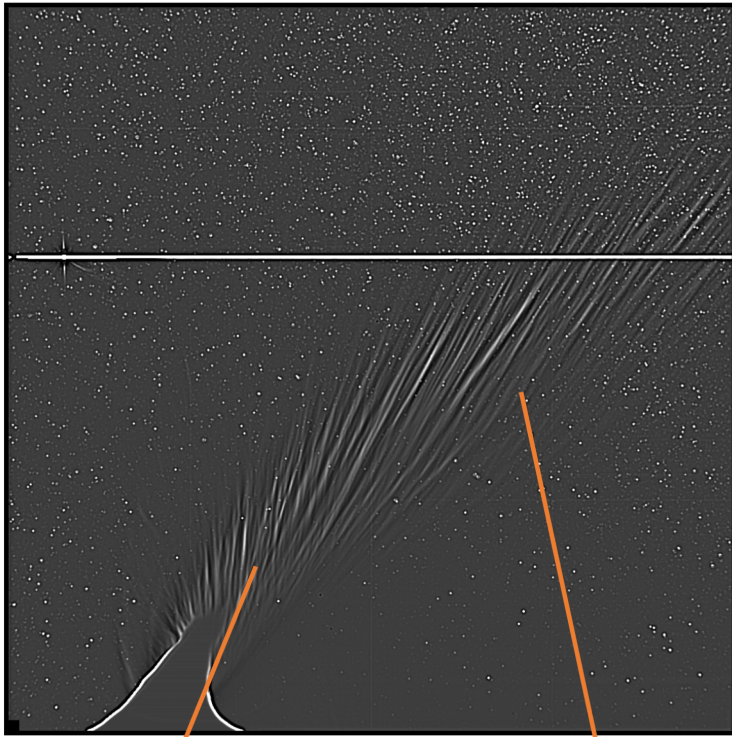


Figure 16: The tail of McNaught on 2007 January 15 at 02:01 UT, as captured by HI-1 on STEREO-A, enhanced by subtracting a gaussian blurred version of the frame. The two insets show the clear difference between (a) the “interleaved” striae towards the south (left) part of the image, and (b) a region where striae remain largely near-parallel towards the north. The progression from near-aligned to interleaved spreads across the whole tail over time, as the comet moves towards the south.

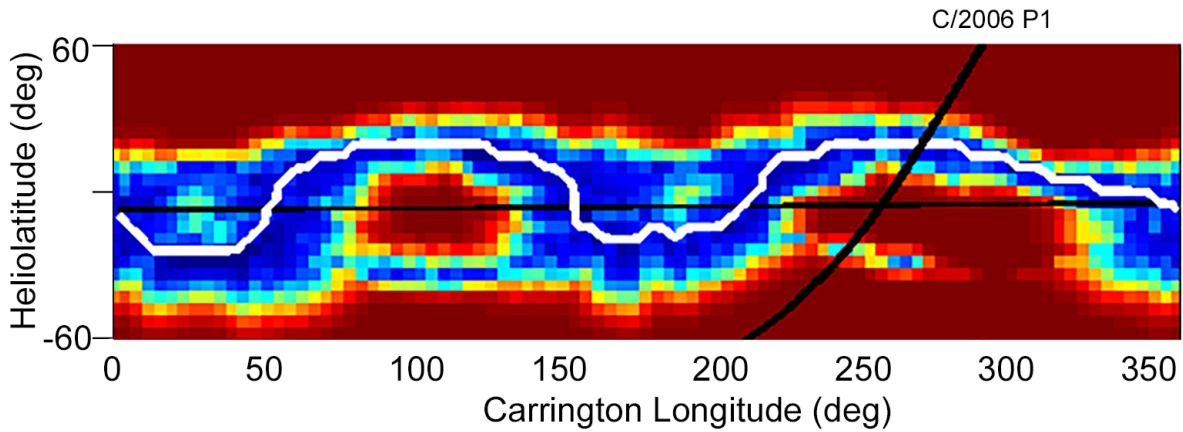


Figure 17: A Mercator projection map of CORHEL modelled solar wind speeds for Carrington rotation 2052 - largely January 2007 - at a distance of 30 solar radii. Speeds range from  $300 \text{ km s}^{-1}$  (dark blue) to  $\sim 750 \text{ km s}^{-1}$  (red). The heliospheric current sheet, HCS, is traced by the white line. The thin black horizontal line shows the sub-Earth position during this solar rotation. McNaught's track is the inclined black line; motion was from north to south. McNaught entered the simulation domain at around 40 solar radii, reached perihelion at 36.7 solar radii on January 12. It then crossed the HCS, moving anti-sunward, and left the model domain at 70 solar radii. After crossing the HCS and surrounding streamer belt, the comet passed through an isolated region of slower solar wind. This fixed distance plot provides a general impression of the solar wind conditions encountered by McNaught. The parameter plots in Figure 18 are more accurate, as they take the comet's changing heliocentric distance into account.

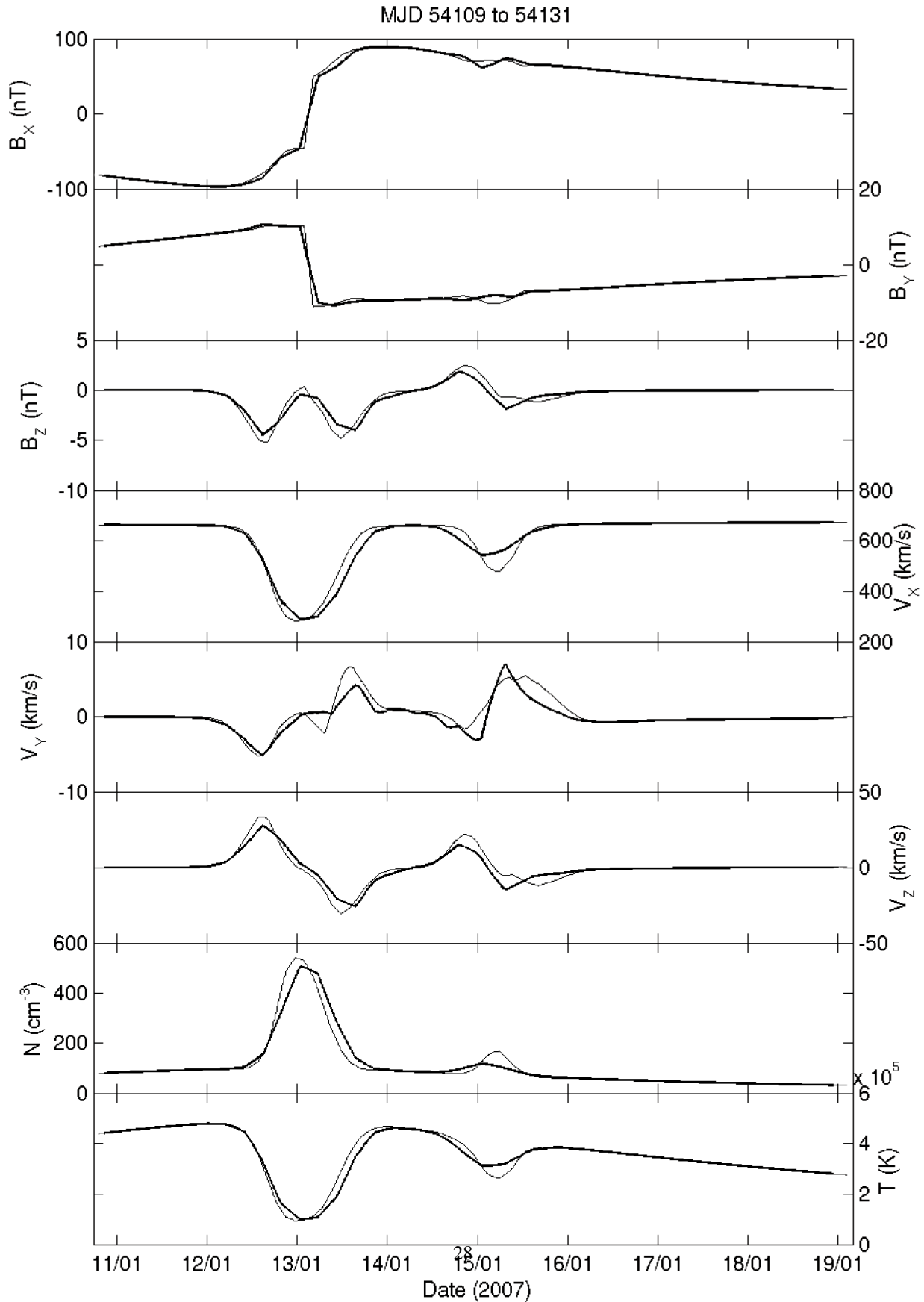


Figure 18: Solar wind conditions at the nucleus of McNaught estimated using the CORHEL model, extracted along the path of McNaught in Figure 17, plotted against date in the format month/day. From top to bottom, the panels show the three components of the heliospheric magnetic field in the Radial-Tangential-Normal coordinate system; three components of the solar wind speed in the same system, the solar wind particle number density, and finally the plasma temperature. The black and grey lines correspond to the two solar magnetogram datasets used.

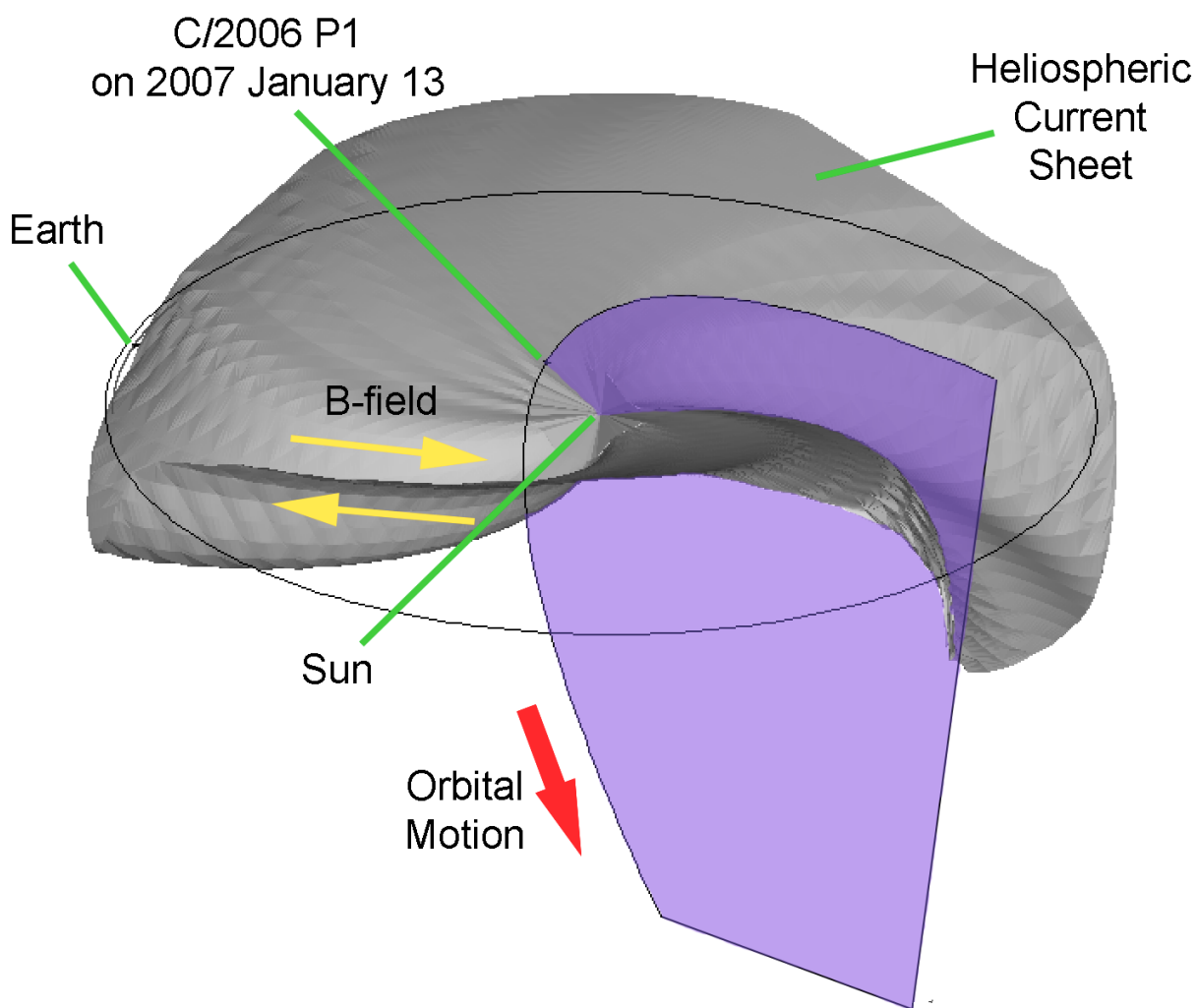


Figure 19: The relative positions of Comet McNaught's orbit and the heliospheric current sheet, HCS, as estimated from the CORHEL model. Yellow arrows denote the general direction of the heliospheric magnetic field to the north and south of the HCS. Earth's orbit at 1 AU from the Sun is shown as a circle. The HCS, comet nucleus, and planet's positions are shown for 2007 January 13.